Three-dimensional XY universality and nonlinear magnetic susceptibility in a kagome ice compound

Kan Zhao, Hao Deng, Hua Chen, Nvsen Ma, Noah Oefele, Jiesen Guo, Xueling Cui, Chen Tang, Matthias J. Gutmann, Thomas Mueller, Yixi Su, Vladimir Hutanu, Changqing Jin, Philipp Gegenwart

Angaben zur Veröffentlichung / Publication details:

Zhao, Kan, Hao Deng, Hua Chen, Nvsen Ma, Noah Oefele, Jiesen Guo, Xueling Cui, et al. 2026. "Three-dimensional XY universality and nonlinear magnetic susceptibility in a kagome ice compound." *Physical Review X* 16 (2): 021043. https://doi.org/10.1103/xl5f-zj9p.

Three-Dimensional XY Universality and Nonlinear Magnetic Susceptibility in a Kagome Ice Compound

Kan Zhao,[1,2,*] Hao Deng,[3,4,5,†] Hua Chen,[6,7,‡] Nvsen Ma,[1,§] Noah Oefele,[2] Jiesen Guo,[1] Xueling Cui,[1] Chen Tang,[1] Matthias J. Gutmann,[8] Thomas Mueller,[9] Yixi Su,[9] Vladimir Hutanu,[5] Changqing Jin,[10,11] and Philipp Gegenwart[2,‖]

[1]*School of Physics, Beihang University, Beijing 100191, China*
[2]*Experimentalphysik VI, Center for Electronic Correlations and Magnetism, University of Augsburg, 86159 Augsburg, Germany*
[3]*State Key Laboratory of Quantum Functional Materials, School of Physical Science and Technology, ShanghaiTech University, Shanghai 201210, China*
[4]*ShanghaiTech Laboratory for Topological Physics, ShanghaiTech University, Shanghai 201210, China*
[5]*Institute of Crystallography, RWTH Aachen University and Jülich Centre for Neutron Science (JCNS) at Heinz Maier-Leibnitz Zentrum (MLZ), Garching, Germany*
[6]*Department of Physics, Colorado State University, Fort Collins, Colorado 80523, USA*
[7]*School of Materials Science and Engineering, Colorado State University, Fort Collins, Colorado 80523, USA*
[8]*ISIS Facility, Rutherford Appleton Laboratory, Chilton, Didcot OX11 0QX, United Kingdom*
[9]*Jülich Centre for Neutron Science (JCNS) at Heinz Maier-Leibnitz Zentrum (MLZ), Forshungszentrum Jülich GmbH, D-85747 Garching, Germany*
[10]*Beijing National Laboratory for Condensed Matter Physics, Institute of Physics, Chinese Academy of Sciences, Beijing 100190, China*
[11]*School of Physical Sciences, University of Chinese Academy of Sciences, Beijing 100190, China*

(Received 5 June 2025; revised 22 January 2026; accepted 1 April 2026; published 26 May 2026)

Kagome spin ice is an intriguing class of spin systems constituted by in-plane Ising spins with ferromagnetic interaction residing on the kagome lattice, theoretically predicted to host a plethora of magnetic transitions and excitations. In particular, different variants of kagome spin ice models can exhibit different sequences of symmetry breaking upon cooling from the paramagnetic to the fully ordered ground state. Recently, it has been demonstrated that the frustrated intermetallic HoAgGe stands as a faithful solid-state realization of kagome spin ice. However, whether any of the established symmetry-breaking pathways apply to this material remains unaddressed. Here, we use single-crystal neutron diffuse scattering to map the spin ordering of HoAgGe at various temperatures more accurately; surprisingly, we find that the ordering sequence appears to be different from previously known scenarios: From the paramagnetic state, the system first enters a partially ordered state with fluctuating magnetic charges, in contrast to a charge-ordered paramagnetic phase, before reaching the fully ordered state. Through Monte Carlo simulations and scaling analyses using an extended three-dimensional (3D) spin model for the distorted kagome spin ice in HoAgGe, we elucidate a single 3D XY phase transition into the ground state with broken time-reversal symmetry (TRS). However, the 3D XY transition has a long crossover tail before the fluctuating magnetic charges fully order. More interestingly, we find, both experimentally and theoretically, that the TRS-breaking phase of HoAgGe features an unusual, hysteretic response: Despite their vanishing magnetization, the two time-reversal partners are distinguished and selected by a nonlinear magnetic susceptibility tied to the kagome ice rule. Our discovery not only unveils a new symmetry-breaking hierarchy of kagome spin ice but also demonstrates the potential of TRS-breaking frustrated spin systems for information technology applications.

DOI: 10.1103/xl5f-zj9p

Subject Areas: Condensed Matter Physics, Nonlinear Dynamics, Strongly Correlated Materials

[*]Contact author: kan_zhao@buaa.edu.cn
[†]Contact author: denghao@shanghaitech.edu.cn
[‡]Contact author: huachen@colostate.edu
[§]Contact author: nvsenma@buaa.edu.cn
[‖]Contact author: philipp.gegenwart@physik.uni-augsburg.de

I. INTRODUCTION

Geometrical frustration in spin systems can result in exotic phases of matter [1–9]. In two dimensions (2D), in-plane Ising spins with dominant nearest-neighbor ferromagnetic coupling on the kagome lattice, known as the kagome spin ice, have been a rich playground for unconventional critical behavior due to frustration [10–31]. If there is only the nearest-neighbor ferromagnetic coupling J_1, the ground state of the model has an extensive entropy of $0.501k_B$ per spin. This degeneracy can be removed with the help of either a second-neighbor interaction J_2 or a long-range dipolar interaction J_{DD} [13–15]; then, the system is ordered into the classic $\sqrt{3}\times\sqrt{3}$ state at the lowest temperature.

Interesting proposals have been made on how the different kagome spin ice models transition into the ground state as temperature decreases. Pioneering analytical and numerical studies have established that varying J_2 vs J_{DD} leads to different symmetry-breaking pathways: A J_1-J_2 model is ordered through a floating Berezinskii-Kosterlitz-Thouless (BKT) critical region separated from the paramagnetic and the ground states by two BKT transitions, whereas a J_1-J_{DD} model goes through a novel magnetic-charge-ordered (MCO) state, bounded by a transition in the universality class of the three-state Potts model at low temperature, as well as an Ising transition at high temperature [13–15]. In the MCO state, the local spins, each viewed as a dipole of magnetic charges, are fluctuating, but the sum of magnetic charges on the two triangular plaquettes of the kagome lattice forms a long-range order, leaving an entropy $0.108k_B$ per spin. The MCO state is a genuine Coulomb phase, reminiscent of the spin ice behavior in pyrochlore $Dy_2Ti_2O_7$ and $Ho_2Ti_2O_7$ systems [32–34].

Kagome spin ice states have been realized in artificial spin ice systems [35–37], in a field-induced stable state in pyrochlore spin ice materials [32–34], and more recently in the intermetallic HoAgGe [16]. In the last case, the strong local easy-axis anisotropy, together with ferromagnetic J_1 of the Ho^{3+} moments, leads to the ice rules on a distorted kagome lattice formed by Ho atoms in each (001) plane. The kagome ice rules in HoAgGe are also consistent with the various phases accessed by varying the magnetic field and temperature. However, the precise nature of the zero-field intermediate phase in HoAgGe and that of the two transitions separating it from the ground and the paramagnetic states are still unclear, despite the experimental and numerical evidence suggesting a partially ordered state, which is different from any of the established scenarios mentioned above.

As another consequence of the kagome ice rules coexisting with non-negligible further-neighbor interactions, at low temperatures, the magnetization of HoAgGe versus external magnetic fields parallel to the kagome plane exhibits a series of plateaus [16,17,24–29]. More recently, it was discovered that an emergent time-reversal-like degeneracy appears at the 1/3 and 2/3 plateaus as revealed by the anomalous Hall effect (AHE) [17,38–45]. However, the ground-state plateau has vanishing AHE and net magnetization due to its antiferromagnetic (AFM) nature, as does the zero-field intermediate phase, making them challenging to characterize by thermodynamic and transport measurements.

Any symmetry-breaking phase, in general, has characteristic response properties. Despite the vanishing magnetization and the AHE, the ground state of HoAgGe hosts other responses that underpin its time-reversal-symmetry (TRS)-breaking nature. In Ref. [17], we showed that the linear magnetoresistance is such a quantity. In this work, we further point out that a unique nonlinear magnetic susceptibility, defined as the second derivative of magnetization with respect to the magnetic field, becomes nonzero in the TRS breaking ground state of HoAgGe.

Discussions of nonlinear magnetic susceptibility can be traced back to 1960s [46,47], when magnetic symmetry became widely used in constraining physical properties of solids. More comprehensive microscopic understandings of nonlinear susceptibility were developed in the 1970s through the case study of dysprosium aluminum garnet ($Dy_3Al_5O_{12}$) [48–52], which has a noncollinear AFM order. Other recent reports of nonlinear susceptibility include that on pyrochlore $Eu_2Ir_2O_7$ [53–55] and $Nd_2Zr_2O_7$ [56,57], which have all-in-all-out spin order. Here, we use the previously established classical spin model to give a minimal microscopic theory of the nonlinear susceptibility of HoAgGe, which also applies to other kagome spin ice systems. Moreover, we argue that the nonlinear susceptibility not only serves as a signature of TRS breaking but also offers an experimental protocol of selecting TRS partners in a large class of antiferromagnetic spin systems.

The rest of the article is organized as follows. Section II elucidates the transition pathways of HoAgGe. In Sec. II A, we first use spin-polarized diffuse neutron scattering to unveil important details of the spin order in HoAgGe at different temperatures. Then, in Sec. II B, through comprehensive Monte Carlo (MC) simulations of an experimentally motivated 3D model and scaling analysis, we establish that the intermediate phase is better characterized as a gradual charge-ordering crossover, following a phase transition at higher temperature in the 3D XY universality class [13–15,58–66]. Section III focuses on macroscopic responses of the TRS breaking phases below the 3D XY transition of HoAgGe. Following a general discussion on the symmetry of nonlinear susceptibility $\chi^{(1)}$ in Sec. III A, in Sec. III B we present thermodynamic and magnetic measurements that reveal the unusual finite and hysteretic $\chi^{(1)}$. A minimal microscopic theory is then given in Sec. III C. Discussions and conclusions are included in Sec. IV.

II. 3D XY CRITICALITY OF HoAgGe

A. Spin-polarized diffuse neutron scattering results

The short-range ice correlations have been established in HoAgGe below 20K through thermodynamic probes [16].

As a sanity check, here we first perform polarized neutron diffuse scattering measurements on coaligned HoAgGe single crystals (see Fig. 13 for experiment setup) above $T_2 = 11.6$ K at 15 K. With neutron dipole moments polarized along the c axis of the HoAgGe crystal, aside from any nuclear contributions, the spin-flip (SF) channel is related to the ab-plane magnetization components dominated by the in-plane Ising spins (see Fig. 13) and should therefore reveal the short-range ice correlation at this temperature, which is indeed the case, as shown in Fig. 1(f): The triangular shape of the diffuse pattern at the K point of the first Brillouin zone indicates the establishment of the kagome ice rule; i.e., there is one magnetic charge per triangular plaquette [see Fig. 1(c)] [18,19]. Below, we name this ice-correlated paramagnetic phase the kagome ice I, or KI. MC simulations using the classical spin model also give similar patterns in KI [see Fig. 1(g)].

The SF diffuse scattering map at 10 K [Fig. 1(e)], below the transition temperature T_2, reveals the emergence of long-range order at K points, corresponding to a $\sqrt{3} \times \sqrt{3}$ magnetic unit cell [see Figs. 1(e) and 2(a)–2(c)]. In this intermediate phase denoted as kagome ice II (KII), the Ho spins are only partially ordered, as seen from the persisting diffuse scattering features. Moreover, magnetic contributions to the neutron intensities at the nuclear sites are vanishingly small, which suggests that the three inequivalent ordered Ising spins in the $\sqrt{3} \times \sqrt{3}$ cell, denoted by $(\bar{\sigma}_{\mathrm{Ho1}}, \bar{\sigma}_{\mathrm{Ho2}}, \bar{\sigma}_{\mathrm{Ho3}})$, must add up to zero (see Appendix E for details). Previously, by assuming a partial order similar to that in Ref. [12], we performed neutron refinement with $(\bar{\sigma}_{\mathrm{Ho1}}, \bar{\sigma}_{\mathrm{Ho2}}, \bar{\sigma}_{\mathrm{Ho3}}) = (\bar{\sigma}, -\bar{\sigma}, 0)$ at 10 K and obtained $\bar{\sigma} = 5.2(1)\mu_B$ (Table I and Fig. S10B in Ref. [16]).

The vanishing total of $(\bar{\sigma}_{\mathrm{Ho1}}, \bar{\sigma}_{\mathrm{Ho2}}, \bar{\sigma}_{\mathrm{Ho3}})$ in KII also means that the ordered spins have zero net magnetic charge per triangle, distinguishing it from the ground state, which has ordered magnetic charge $\bar{Q}_m = \pm 1$ per triangle. The KII phase is therefore characterized by a "divergence-free" triad of $(\bar{\sigma}_{\mathrm{Ho1}}, \bar{\sigma}_{\mathrm{Ho2}}, \bar{\sigma}_{\mathrm{Ho3}})$ which breaks lattice translation symmetry but still has fluctuating magnetic charges [20]. Compared to the charge-ordered phase in dipolar kagome ice [13–15], which can be described using the above quantities as $\bar{Q}_m = \pm 1$ and $\bar{\sigma}_{\mathrm{Ho1}} = \bar{\sigma}_{\mathrm{Ho2}} = \bar{\sigma}_{\mathrm{Ho3}} = 0$, KII

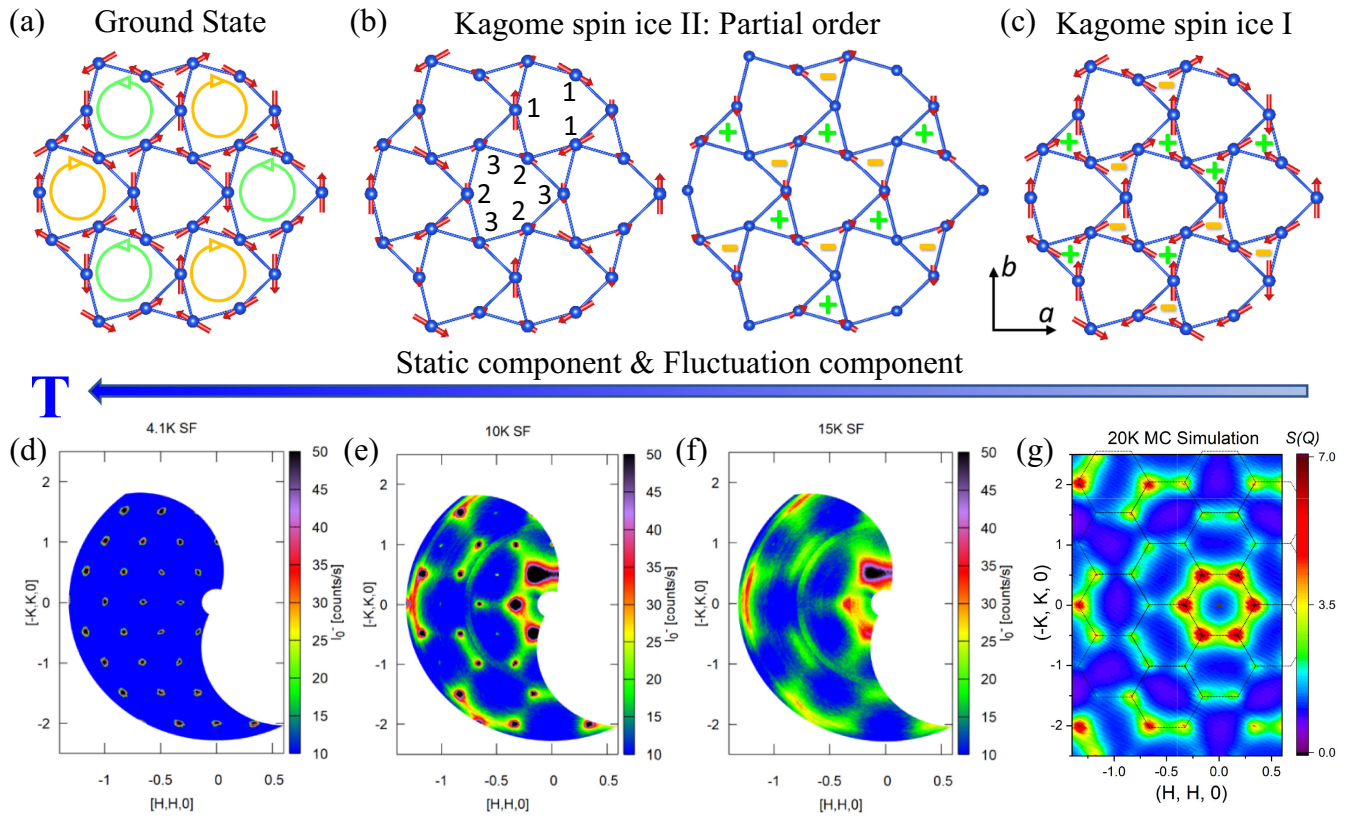

FIG. 1. Multistage ordering behavior under changing temperature in kagome spin ice HoAgGe. (a) Illustration of magnetic structure of the fully ordered ground state. (b) Kagome ice II: partial order, including static component with $(\bar{\sigma}/2, \bar{\sigma}/2, -\bar{\sigma})$ order and related fluctuation component. (c) Kagome ice I: short-range correlation state, with the definition of the a and b directions in panels (a)–(c) and the three inequivalent Ho sites Ho1, Ho2, and Ho3 labeled by 1, 2, and 3, respectively, for simplicity. The SF channel of polarized neutron diffuse scattering reveals magnetic correlations of HoAgGe in the ab plane at 4 K (d), 10 K (e), and 15 K (f), together with the structure factor $S(Q)$ for the kagome ice I state at $T = 20$ K (g) from MC simulations based on the quasi-2D spin model (see text). The schematics of the Brillouin zones contain the vertices of a hexagon, shown as K points.

has $\bar{Q}_m = 0$ and $\bar{\sigma}_{\mathrm{Ho1}} + \bar{\sigma}_{\mathrm{Ho2}} + \bar{\sigma}_{\mathrm{Ho3}} = 0$, although the fluctuating spins still obey the ice rule as depicted in Fig. 1(b).

We note that $(\bar{\sigma}_{\mathrm{Ho1}}, \bar{\sigma}_{\mathrm{Ho2}}, \bar{\sigma}_{\mathrm{Ho3}}) = (\bar{\sigma}, -\bar{\sigma}, 0)$ is not the only possibility that satisfies the above constraint. We refine the elastic magnetic neutron data at 10 K using the $(\bar{\sigma}/2, \bar{\sigma}/2, -\bar{\sigma})$ and $(\bar{\sigma}/3, 2\bar{\sigma}/3, -\bar{\sigma})$ states [see Figs. 2(b) and 9] that have the same magnetic space group (MSG), and we obtain almost identical refinement factors R and wR as in the previous case but with $\bar{\sigma} = 6.0(1)\mu_B$ and $5.9(1)\mu_B$, respectively. In fact, any ordered states that fulfill the divergence-free constraint would yield virtually the same refinement factors.

As the temperature continues to decrease below 10 K, the neutron diffuse scattering intensities gradually disappear, accompanied by the increase of magnetic contributions at the nuclear sites, as shown in Figs. 1(d) and 2(a). Despite being small, the magnetic contribution at nuclear site (2, −1, 0) arises below T_2, while its behavior resembles a power-law spin correlation in the vicinity of $T_1 \sim 7$ K [see Fig. 2(a)]. At 4 K, the system reaches its ground state $(\bar{\sigma}, \bar{\sigma}, -\bar{\sigma})$, with the ordered spin $\bar{\sigma} = 7.5(1)\mu_B$ [see Figs. 1(a) and 2(b)] [16]. The evolution of T_1 and T_2 transitions under magnetic fields H$\|b$ is shown in the phase diagram in Fig. 2(f) based on low-temperature magnetic specific heat C_{mag} in Figs. 2(d) and 2(e).

B. Monte Carlo simulation and scaling analysis

To understand the critical behavior of HoAgGe revealed from neutron and previous thermodynamic experiments, we first resort to the 2D classical spin model introduced in Ref. [16]:

$$H = J_1 \sum_{nn} \sigma_i \sigma_j + J_2 \sum_{nnn_1} \sigma_i \sigma_j + J_4 \sum_{nnn_2} \sigma_i \sigma_j + J_3 \sum_{tnn} \sigma_i \sigma_j + \sum_{\langle i,j \rangle} E_d(i,j), \quad (1)$$

where $\sigma_i = \pm 1$ is an Ising variable on site i. As shown in Fig. 3(a), J_1 stands for the nearest-neighbor (nn) antiferromagnetic Ising coupling, while J_2 and J_4 both originate from the next-nearest-neighbor (nnn) coupling on the ideal kagome lattice but become different here due to the rotation of the triangular plaquettes. Note that J_3 stands

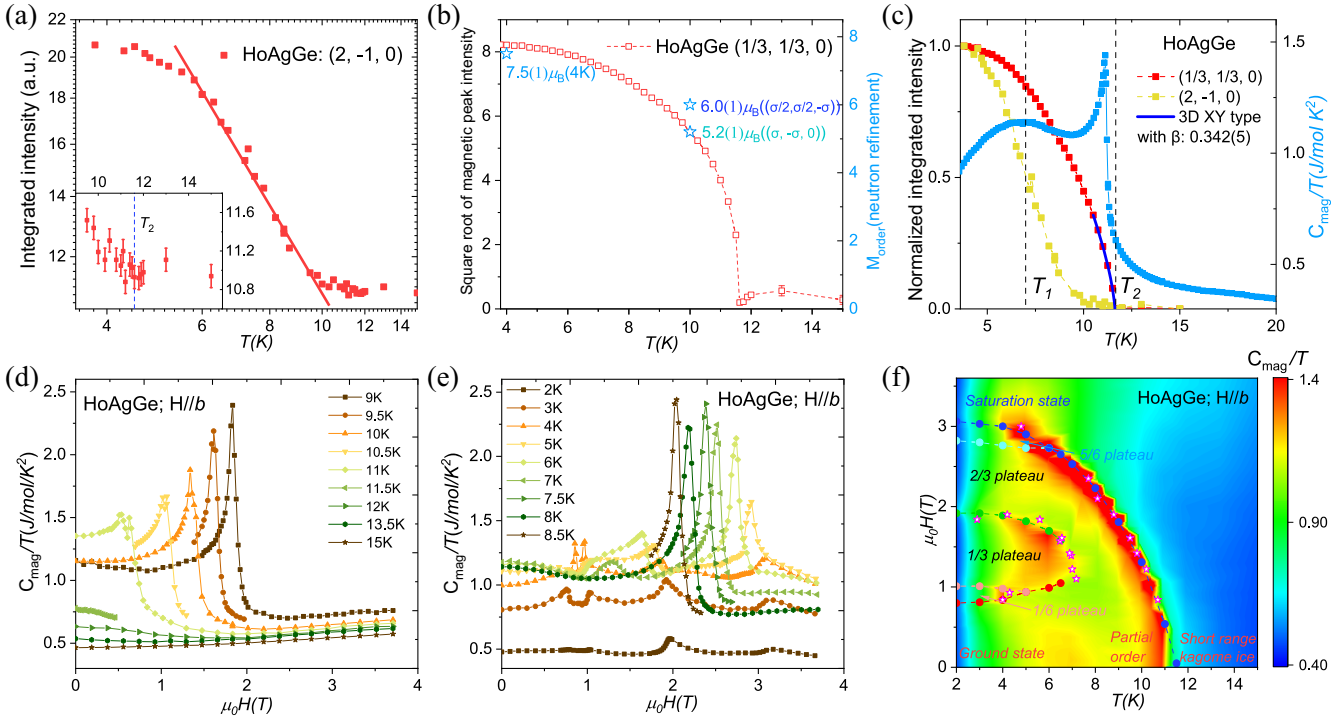

FIG. 2. Magnetic specific heat and neutron diffraction results of HoAgGe. (a) Integrated intensity of nuclear site (2, −1, 0) from 15 K down to 3.8 K, with solid lines representing a linear fitting to log-log data points between 6 K and 10 K [inset shows integrated intensity of nuclear site (2, −1, 0) from 15 K down to 9.5 K] (b) Square root of integrated intensity of magnetic peak (1/3, 1/3, 0) from 15 K down to 3.8 K, with the Ho ordered moment derived from neutron refinement on the right side (see text). (c) Integrated intensity of the magnetic peak (1/3, 1/3, 0) and nuclear site (2, −1, 0) from 15 K down to 3.8 K according to the neutron diffraction, and the magnetic specific heat C_{mag}/T of HoAgGe from 20 K down to 2 K, with the dotted lines indicating the onset of T_1 and T_2 (see text). (d),(e) Field dependence of the magnetic specific heat C_{mag} under H$\|b$ with various temperatures, respectively. (f) H-T phase diagram of HoAgGe under H$\|b$ as derived from $M(H)$ (filled circles) and C_{mag} and Γ_H (empty stars) measurements (see Ref. [17]), with the color coding represents the magnetic specific heat C_{mag}/T (see text).

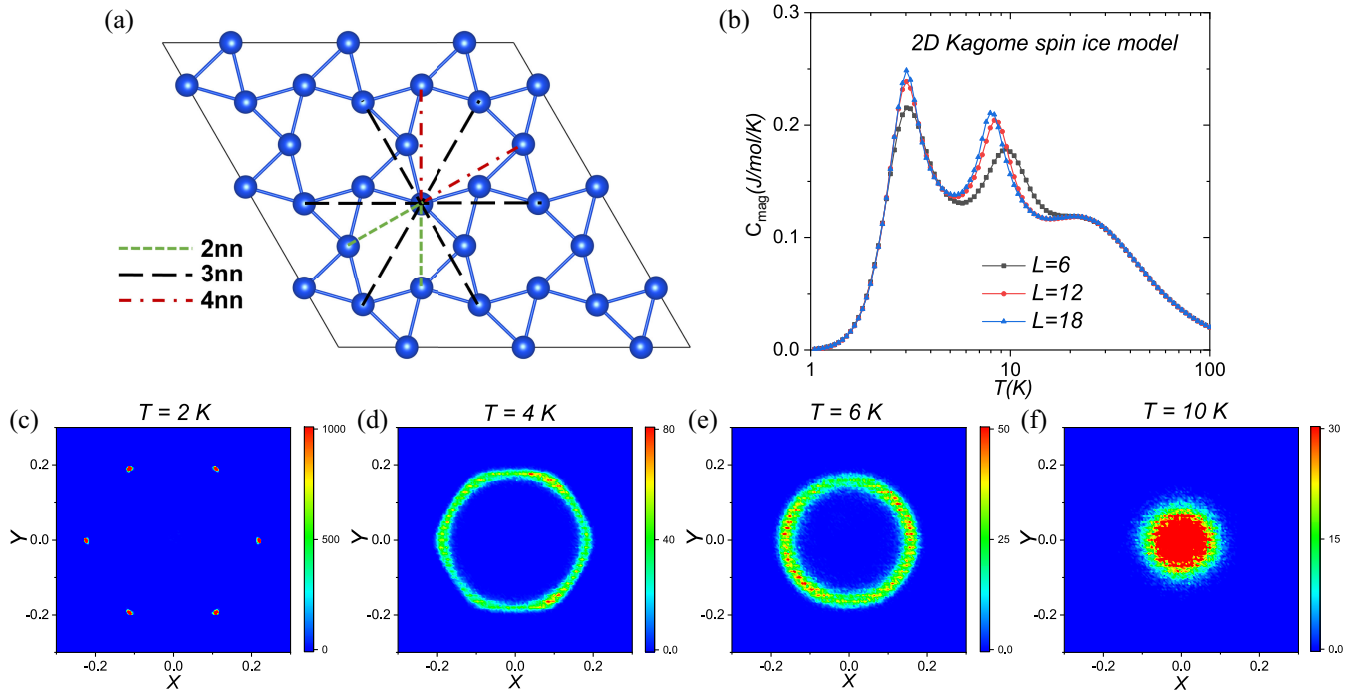

FIG. 3. MC simulated physical property and order parameter symmetry analysis based on the 2D spin model. (a) In-plane nearest neighbors on the distorted kagome lattice of HoAgGe. (b) Monte Carlo simulated magnetic specific heat C_{mag}, based on the 2D spin model here with various lattice size. The distribution of the complex-order parameter M defined in Eq. (2) based on the 2D spin model with 18×18 lattice size at $T = 2$ K (c), $T = 4$ K (d), $T = 6$ K (e), and $T = 10$ K (f), respectively.

for the interactions between third-nearest neighbors (tnn); $E_d(i,j)$ is the magnetic dipolar interaction between two spins on sites i and j [see Eq. (S2) in Ref. [16]]; and $J_1 - J_4$ absorbs the dot products of Ising axis unit vectors of different pairs. Consequently, $J_1 = 1.0$ meV, $J_2 = -0.115$ meV, $J_3 = 0.127$ meV, $J_4 = -0.0635$ meV [16].

Figure 3(b) presents the MC-simulated magnetic specific heat C_{mag} curves derived from the 2D spin model for various lattice sizes. In addition to the high-temperature anomaly observed around 22 K, a magnetic transition at $T_1 = 3.0$ K exhibits weak dependence on system size, whereas a distinct sharp peak emerges at $T_2 = 9.5$ K, 8.3 K, and 8.0 K for lattice sizes $L = 6$, 12, and 18, respectively, consistent with previous results [16].

To gain a deeper understanding of the universality class of the transition at T_1 and T_2, we consider the complex-order parameter M [15,22],

$$M = \frac{1}{N}\sum_{i=1}^{N} \sigma_i \exp(i\vec{Q}\cdot\vec{r}_i), \tag{2}$$

with N the total number of spins and $\vec{Q} = \{[(4\pi)/3], 0\}$. The sixfold degenerate ground states are captured by the discrete phase of $M = |M|e^{i\phi}$, with $\phi = [(n\pi)/3]$ and integer $0 \le n \le 5$ [15,22], as shown in Fig. 3(c), which plots the histogram of M at 2 K on the complex plane (the 2D MC simulations were performed on the ideal kagome lattice).

At 6 K, the histogram of M is distributed around a circle centered at the origin in Fig. 3(e), consistent with the $U(1)$ symmetry in the J_1-J_2 model [15,22]. Thus, the 2D model is ordered through a floating Berezinskii-Kosterlitz-Thouless (BKT) critical region separated from the paramagnetic and the ground states by two BKT transitions at $T_1 = 3$ K and $T_2 \sim 8$ K, similar to the J_1-J_2 model case [15,22].

The pure 2D model above corresponds to the limiting situation where the intra-ayer ferromagnetic coupling between the kagome layers approaches infinity. In reality, the interlayer distance $d_c = 4.1864$ Å is larger than the intralayer nearest-neighbor distance $d_1 = 3.6860$ Å but smaller than the second-nearest-neighbor distance $d_2 = 5.1207$ Å [16]. Given the RKKY nature of magnetic interactions in metallic HoAgGe, it is expected that the intralayer exchange coupling J_c falls between J_1 and J_2 and therefore has important influences on the critical behavior of the 3D system.

We therefore generalize Eq. (1) to a 3D model by additionally including an interlayer exchange coupling J_c:

$$H = J_1\sum_{nm}\sigma_i\sigma_j + J_2\sum_{nnn_1}\sigma_i\sigma_j + J_4\sum_{nnn_2}\sigma_i\sigma_j + J_3\sum_{tnn}\sigma_i\sigma_j + J_c\sum_{cnn}\sigma_i\sigma_j + \sum_{\langle i,j\rangle}E_d(i,j). \tag{3}$$

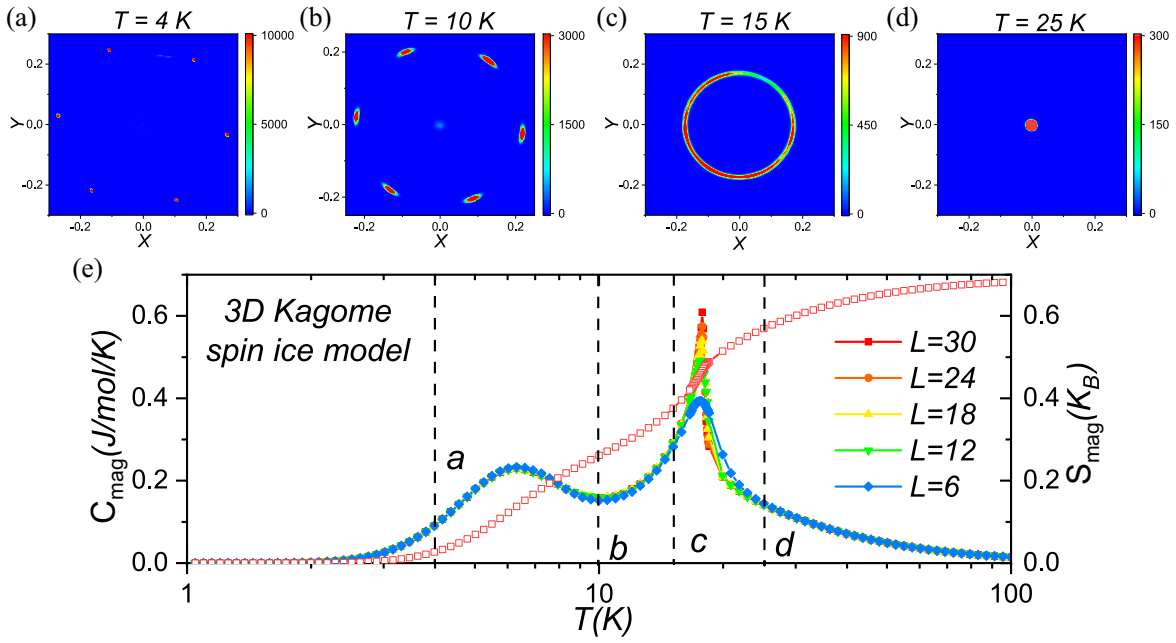

FIG. 4. MC simulated physical property and order parameter symmetry analysis based on the 3D spin model. (e) Simulated low-temperature magnetic specific heat C_{mag} and entropy S_{mag} curve with lattice size $L = 6$, 12, 18, 24, and 30 (see text). The distribution of the complex-order parameter M defined in Eq. (2) is shown at various temperatures, $T = 4$ K (a), $T = 10$ K (b), $T = 15$ K (c), and $T = 25$ K (d).

During the classical MC simulations (see Appendix D for details), J_c has been fixed to -0.27 meV to ensure that each kagome layer maintains identical spin ordering in the ordered phases. Consequently, the 3D spin system exhibits the same in-plane field-induced magnetization plateaus as the 2D model described in Ref. [16]. The MC simulations are performed on three-dimensional lattices of size $L \times L \times L$, where the third L is along the c axis.

Specific heat C_{mag} from our MC simulations [Fig. 4(e)] clearly exhibits two features: A sharp peak appears at $T_2 = 17.8$ K, with obvious system-size dependence; another broad anomaly starts below 10 K and centers at $T_1 = 6.5$ K, insensitive to system sizes. The two specific heat features qualitatively agree with that in the experimental data [Fig. 2(c)]. In addition, the entropy S_{mag} in Fig. 4(e) decreases from $0.693k_{\mathrm{B}}$ per spin of the Ising paramagnet to $0.52k_{\mathrm{B}}$ per spin around 20 K, indicative of the short-range ice order and consistent with the magnetic structure factor $S(Q)$ data in Fig. 1(g). After T_2, S_{mag} quickly decreases to $0.262k_{\mathrm{B}}$ per spin at 10 K and eventually approaches zero after the broad anomaly in C_{mag} around T_1.

The peak values of the C_{mag} at T_2 show saturation as the size of the system increases. Therefore, the critical exponent α is expected to be a small, negative value, reminiscent of the $\alpha = -0.02$ of the 3D XY model [58,59]. A finite-size scaling analysis with the 3D XY critical exponents $\alpha = -0.02$ and $v = 0.67$ indeed shows reasonable data collapse close to T_2 [Fig. 5(a)].

To understand why the transition at T_2 is of 3D XY universality, we further investigate the order parameter at varying temperatures. First, consider the complex-order parameter M. The sixfold degenerate ground states are captured by the discrete phase of M with $\phi = [(n\pi/3)]$ and integer $0 \leq n \leq 5$ [15,22], as shown in Fig. 4(a), which plots the histogram of M at 4 K on the complex plane. (The phase angle ϕ is slightly tilted away from $n\pi/3$ due to the distorted kagome lattice of our model.)

At 15 K, the histogram of M in Fig. 4(c) is distributed around a circle centered at the origin, yet not evenly, distinct from the emergent $U(1)$ symmetry in the 2D model above. From 15 K to 10 K, the circle falls into one of six maximum regions in the clock phase [see Fig. 4(b)] and eventually to the six sharp peaks at 4 K.

The finite $|M|$ of the histogram at 15 K suggests that long-range order with nonzero ordered local spins is forming but cannot be fully established due to the competition between many (more than six) degenerate states, corresponding to different values of ϕ around the circle. Such behavior indeed suggests an XY order parameter with weak sixfold anisotropy.

The precise form of the anisotropy for the XY order parameter at $T < T_2$ determines which spin order, characterized by $(\bar{\sigma}_{\mathrm{Ho1}}, \bar{\sigma}_{\mathrm{Ho2}}, \bar{\sigma}_{\mathrm{Ho3}})$, is favored. In particular, in the event that the anisotropy changes between different sets of clock orientations [15,21], a first-order phase transition may still occur. To address this issue, we introduce a triad

of ordered Ising variables $(\sigma_1, \sigma_2, \sigma_3)$ (see below and Appendix E for details) analogous to the experimental $(\bar{\sigma}_{\mathrm{Ho1}}, \bar{\sigma}_{\mathrm{Ho2}}, \bar{\sigma}_{\mathrm{Ho3}})$ to study the weakly anisotropic XY order below T_2. A benefit of $(\sigma_1, \sigma_2, \sigma_3)$ compared to M is that it can be defined locally in each magnetic unit cell and can, e.g., help map out domains of favored clock states in real space.

Subject to the constraint of vanishing magnetic charge, $(\sigma_1, \sigma_2, \sigma_3)$ can be represented by points on a ternary plot. Specifically, we define rescaled variables $\tilde{\sigma}_\alpha \equiv [(\sigma_\alpha + 1)/3]$ so that $\tilde{\sigma}_1 + \tilde{\sigma}_2 + \tilde{\sigma}_3 = 1$. A ternary plot for $(\tilde{\sigma}_1, \tilde{\sigma}_2, \tilde{\sigma}_3)$ has three corners of the equilateral triangle corresponding to (1, 0, 0) and their permutations. The $\tilde{\sigma}_\alpha$ coordinate of any point inside the triangle is the ratio of the height of the point, measured from the edge opposed to the α-th vertex and the triangle height. In this representation, the $(\bar{\sigma}, -\bar{\sigma}, 0)$ phase corresponds to the $(\frac{1}{3}, \frac{2}{3}, 0)$ point and its equivalent on the ternary plot [Fig. 5(b)]. Mappings of $(\bar{\sigma}/2, \bar{\sigma}/2, -\bar{\sigma})$ and $(\bar{\sigma}/3, 2\bar{\sigma}/3, -\bar{\sigma})$ discussed above are illustrated in Fig. 5(c). Figures 5(d) and 5(e) depict the ternary plots for the intermediate state at 10 K (see Fig. 18) averaged over 1000 and 5000 steps, respectively. Apparently, the anisotropy leans more towards that of $(\bar{\sigma}/2, \bar{\sigma}/2, -\bar{\sigma})$ and $(\bar{\sigma}/3, 2\bar{\sigma}/3, -\bar{\sigma})$ than $(\bar{\sigma}, -\bar{\sigma}, 0)$. The former two states are therefore more likely to describe the KII phase of HoAgGe.

Since the emergent $U(1)$ symmetry is fully broken at T_2, there should not be additional second-order phase transitions below T_2. Moreover, since the form of sixfold anisotropy is consistent with that of the ground state, no first-order transitions are expected below T_2 either. Therefore, the broad anomaly of C_{mag} at T_1 should be a crossover, during which the remnant fluctuating spin components in the divergence channel become ordered but without a symmetry change. On the one hand, this case is supported by the rather weak sample-size dependence of the T_1 specific heat peak. On the other hand, the structure factor $S(Q)$ from our MC simulations also has vanishing intensities at the nuclear sites at 15 K, but the latter gradually become finite at 10 K (Fig. 17), consistent with experimental results. The above MC results and scaling analysis provide concrete evidence supporting the 3D XY universality in our quasi-2D model as well as in HoAgGe.

Since the ground state and KII have the same symmetry and, in particular, both break TRS, they should have similar

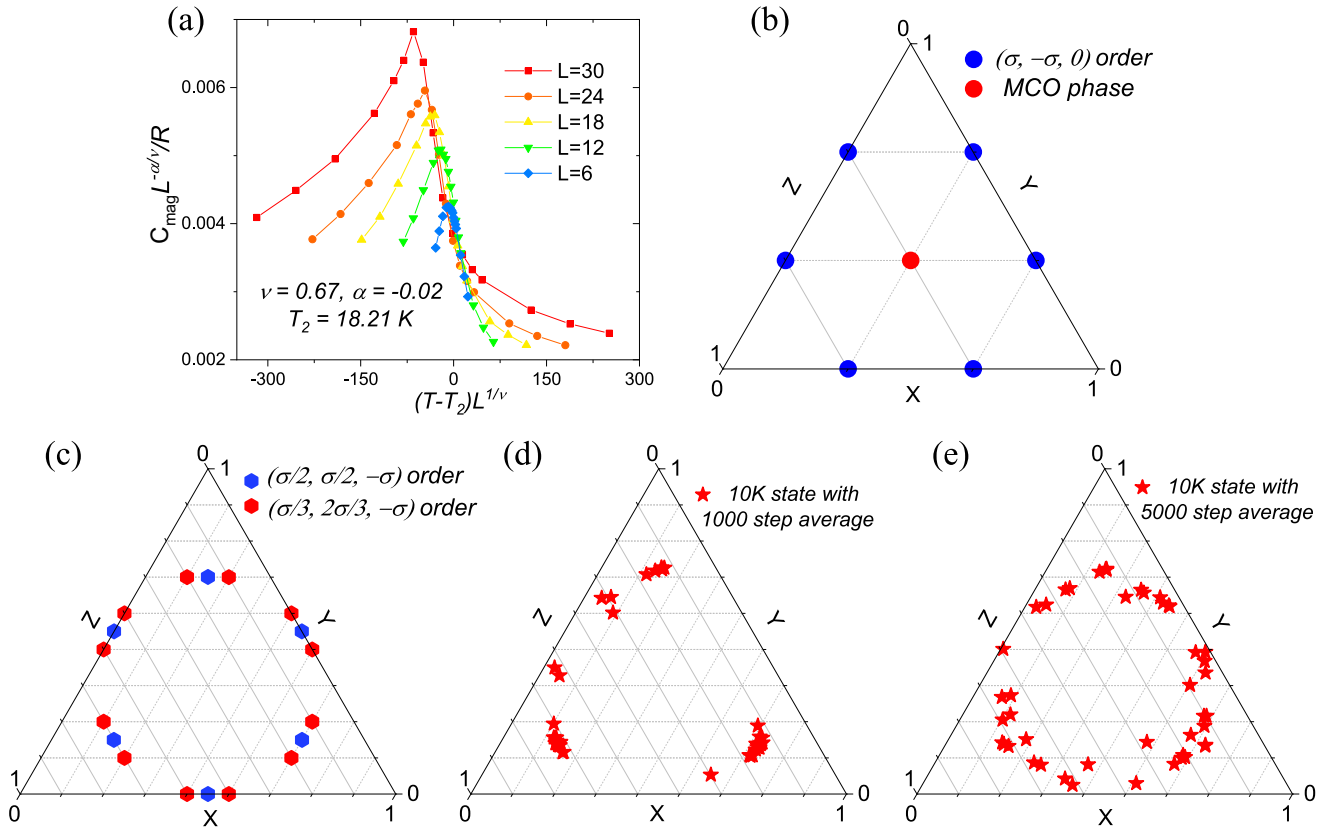

FIG. 5. Monte Carlo simulation of the kagome ice II state and phase transition at T_2. (a) Scaling of specific heat C_{mag} near the T_2 transition using critical exponents $\alpha = -0.02$ and $\nu = 0.67$ expected from that of the 3D XY universality class (see text), with lattice size L from 6 to 30. Ternary plots of $(\tilde{\sigma}_1, \tilde{\sigma}_2, \tilde{\sigma}_3)$ for (b) MCO phase and $(\bar{\sigma}, -\bar{\sigma}, 0)$ order; (c) $(\bar{\sigma}/3, 2\bar{\sigma}/3, -\bar{\sigma})$ and $(\bar{\sigma}/2, \bar{\sigma}/2, -\bar{\sigma})$ order; and the intermediate state of our kagome ice model at 10 K, with an average of (d) 1000 steps and (e) 5000 steps from the Monte Carlo simulations.

time-reversal-odd response functions. In the next section, we discuss the nonlinear magnetic susceptibility as such a response.

III. NONLINEAR SUSCEPTIBILITY DUE TO TRS BREAKING

A. Relevance of nonlinear susceptibility to TRS breaking

For a TRS-breaking state, if its TRS partner is not equivalent to itself up to a translation, i.e., its magnetic point group does not involve time reversal $\mathcal{T}$, the two states are distinguishable, in the sense that certain macroscopic measurements involving averaging over unit cells can, in principle, distinguish them. Moreover, if a TRS-breaking state has exactly vanishing net magnetization but finite nonlinear magnetic susceptibilities, it can even be switched by an external magnetic field into its partner state.

Specifically, magnets that can be switched between two TRS partner states by a uniform magnetic field must have different energies in the presence of the magnetic field:

$$F[\mathbf{M}(\mathbf{r}),\mathbf{B}] \neq F[-\mathbf{M}(\mathbf{r}),\mathbf{B}] = F[\mathbf{M}(\mathbf{r}),-\mathbf{B}], \quad (4)$$

where F is the free energy of the system and $\mathbf{M}(\mathbf{r})$ stands for the microscopic magnetization field that breaks time-reversal symmetry. Therefore, by expanding F into power series of $\mathbf{B}$,

$$\begin{aligned} F &= F_0 + \frac{\partial F}{\partial B_{i_1}} B_{i_1} + \frac{1}{2}\frac{\partial^2 F}{\partial B_{i_1}\partial B_{i_2}} B_{i_1}B_{i_2} \\ &\quad + \frac{1}{3!}\frac{\partial^3 F}{\partial B_{i_1}\partial B_{i_2}\partial B_{i_3}} B_{i_1}B_{i_2}B_{i_3} + \ldots \\ &\equiv F_0 - M_{i_1}B_{i_1} - \frac{1}{2}\chi^{(0)}_{i_1 i_2} B_{i_1}B_{i_2} - \frac{1}{3!}\chi^{(1)}_{i_1 i_2 i_3} B_{i_1}B_{i_2}B_{i_3} - \ldots, \end{aligned} \quad (5)$$

where $\chi^{(0)}$ is the usual magnetic susceptibility at zero magnetic field, and $\chi^{(n)}$ with $n > 0$ denotes higher-order nonlinear susceptibilities, at least some odd-power terms must be finite. If the uniform magnetization $\mathbf{M} = 0$, the above condition requires certain $\chi^{(2n+1)}$, with n a non-negative integer. Clearly, $\chi^{(2n+1)} = 0$ if the system has time-reversal symmetry $\mathcal{T}$. Since $\mathbf{B}$ is a pseudovector and does not change under spatial inversion $\mathcal{I}$, $\chi^{(2n+1)} = 0$ if the system has combined $\mathcal{TI}$ symmetry as well.

Besides these simple twofold symmetry operations that change all $\mathbf{B}$ components identically, other space group operations will at least change some components of $\mathbf{B}$ differently from others and would therefore not completely forbid all components of $\chi^{(2n+1)}$. Below, we particularize to the case of applying magnetic fields along a high-symmetry direction, chosen as x without loss of generality, and $\chi^{(1)}$. In addition to $\mathcal{T}$ and $\mathcal{TI}$, a special class of magnetic point group symmetry operations are binary transformations including twofold proper rotation, mirror reflection, and those combined with time reversal, which preserve the indices of tensors up to a sign. The transformation properties of $\chi^{(1)}_{xxx}$ under these four classes of operations are summarized in Table I. One can see that $\chi^{(1)}_{xxx}$ is forbidden by $C_{2y,z}, m_{y,z}, C_{2x}\mathcal{T}, m_x\mathcal{T}$. Namely, there cannot be any twofold axes perpendicular to x or mirror planes parallel to x if not considering time reversal, which will swap the perpendicular and parallel conditions.

TABLE I. Sign factor of $\chi^{(1)}_{xxx}$ transformed by a few binary magnetic space group operations involving twofold rotations.

Operation	$\hat{a}\|\hat{x}$	$\hat{a}\perp\hat{x}$
C_{2a}	+	−
m_a	+	−
$C_{2a}\mathcal{T}$	−	+
$m_a\mathcal{T}$	−	+

For the ground state as well as the KII state of HoAgGe, which has the magnetic space group P-6′m2′ (187.212), the allowed components of $\chi^{(1)}$ are [65–67]

$$\chi^{(1)}_{bbb} = -\chi^{(1)}_{aab} = -\chi^{(1)}_{aba} = -\chi^{(1)}_{baa} \equiv \chi^{(1)}_b. \quad (6)$$

Namely, there is only one free parameter $\chi^{(1)}_b$, and $\chi^{(1)}$ is effective only when the magnetic field is parallel to the ab plane. To verify Eq. (6) explicitly, we note that P-6′m2′ has a mirror plane m_{100}, i.e., a mirror plane perpendicular to the [100] (or b) axis. This symmetry forbids, according to Table I, $\chi^{(1)}_{aaa}$ and $\chi^{(1)}_{ccc}$, but it allows $\chi^{(1)}_{bbb}$. Similarly, P-6′m2′ also has $m_{001}\mathcal{T}$, which forbids $\chi^{(1)}_{ccc}$ but allows $\chi^{(1)}_{bbb}$ and $\chi^{(1)}_{aaa}$. This finding is consistent with the experimental observation that the zero-field hysteresis of $\chi^{(1)}$ only shows up for $\mathbf{H}\|b$ but vanishes for $\mathbf{H}\|a$ [see Figs. 8(c) and 11].

The above symmetry analysis also allows us to obtain the angular dependence of zero-field $\chi^{(1)}$ along the direction of $\mathbf{H}$ rotating in the ab plane:

$$\begin{aligned} \chi^{(1)}_{\phi} &= R_{bi}R_{bj}R_{bk}\chi^{(1)}_{ijk} \\ &= \cos\phi(\cos^2\phi - 3\sin^2\phi)\chi^{(1)}_b, \end{aligned} \quad (7)$$

where R stands for the rotation matrix about c axis by angle $-\phi$. For example, $\chi^{(1)}_{\phi}$ is equal to $1, -1, 0$ at $\phi = 0, \pi/3, \pi/2$, as shown in Fig. 8(b).

B. Experimental evidence of TRS breaking below T_2

Following the above symmetry analysis, in this section, we present experimental results of magnetometry as well as magnetostriction measurements under varying $\mathrm{H}\|b$ around zero field. Figures 6(a)–6(d) summarize field- and

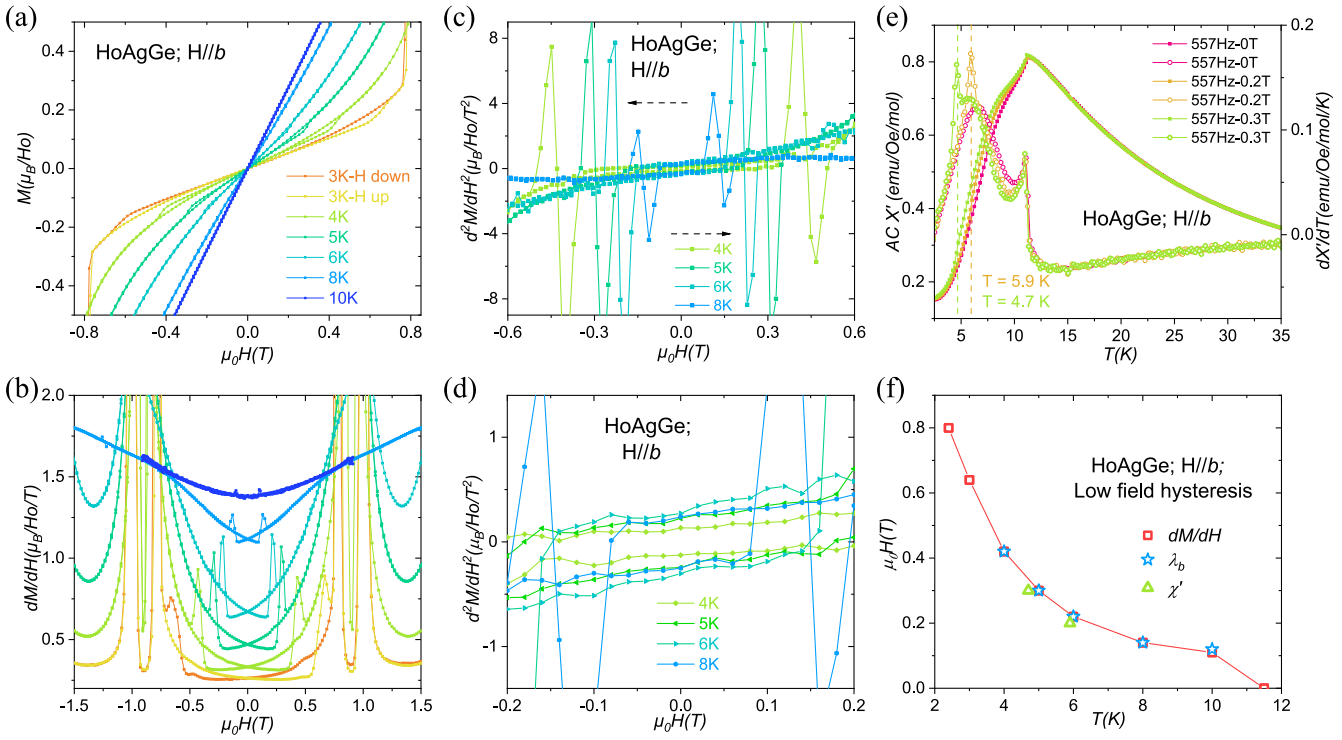

FIG. 6. Magnetization and ac susceptibility of HoAgGe under H$\|b$. (a) Magnetization M, (b) its derivative dM/dH, and (c), (d) its second derivative d^2M/dH^2 curves of HoAgGe under H$\|b$ with both H increasing and decreasing conditions at various temperatures. (e) The ac susceptibility $\chi'(T)$ of HoAgGe with 557 Hz for H$\|b$ under 0, 2000 Oe, and 3000 Oe. (f) Field and temperature dependence of low field hysteresis for HoAgGe under H$\|b$ as derived from $M(H)$ (empty squares), λ_b (empty stars), and ac susceptibility χ' (empty triangles) measurements (see text).

temperature-dependent magnetization M, its derivative dM/dH and second derivative d^2M/dH^2 data (see Fig. 10 for details). First of all, the absence of net M at zero field under field sweeps between ± 2.25 T is consistent with the AFM nature of the ground state. However, pronounced hysteretic behavior is observed in M, dM/dH, and d^2M/dH^2 curves below 10 K, particularly with $\chi^{(1)} = d^2M/dH^2$ having finite values at zero field. As depicted in Fig. 10, the hysteretic signal merges into the phase boundary of 1/6 plateau under $\mu_0 H_b = 0.8$ T at 2.4 K [see Figs. 2(f) and 10(d)]. The coercive field of hysteresis significantly decreases with increasing temperature, reaching $\mu_0 H_b = 0.12$ T at 10 K, reminiscent of the finite magnetic contributions at nuclear site (2, −1, 0) below T_2 [see Fig. 2(a)]. The field and temperature dependence of the hysteretic peaks in dM/dH curves (see Fig. 10) is summarized in Fig. 6(f).

We next focus on the temperature dependence of $\chi^{(1)}$. As shown in Fig. 8(d), it increases from $0.245\mu_B/\mathrm{Ho}/T^2$ at 8 K to the max value $0.287\mu_B/\mathrm{Ho}/T^2$ at 6 K, then gradually decreases to $0.017\mu_B/\mathrm{Ho}/T^2$ at 2.4 K. The appearance of the $M(H)$ hysteresis below T_2 is critically connected to the zero-field $\chi^{(1)}$ (i.e., $\chi^{(1)}_{bbb}$) since such a nonlinear susceptibility breaks the degeneracy of the two TRS partners of the ground state under a weak magnetic field H$\|b$, in spite of the vanishing net magnetization of both states [46–57]. We note the zero-field $\chi^{(1)}$ has a similar temperature dependence as that of $d\chi/dT$ measured under a 500 Oe field, the origin of which deserves future investigation.

Intriguingly, the low field hysteretic signature is also observed in the relative length change $\Delta L/L$ and its field derivative $d(\Delta L/L)/dH$, i.e., magnetostriction λ_b, under H$\|b$ (see Fig. 7). Sweeping fields from +4 T to −4 T, the metamagnetic transitions between the ground state, 1/6 plateau, 1/3 plateau, 2/3 plateau, and saturated states are accompanied by large λ_b peaks due to the first-order nature of such transitions below 4 K. In particular, λ_b becomes as large as 1.5×10^{-4}/T (between the ground state and the 1/6 plateau) and 2.1×10^{-4}/T (between the 1/3 and 2/3 plateau), comparable with that in the isostructural heavy-fermion AFM CePdAl and YbAgGe [68,69].

With increasing temperature, the change of the height and sharpness of the λ_b peaks suggests an evolution from first- to second-order transitions. This suggestion is consistent with the magnetic specific heat C_{mag}/T data with prominent peaks near the metamagnetic transitions below T_2 [see Figs. 2(d)–2(f)], which are notably suppressed below 4 K. In short, both C_{mag} and λ_b data demonstrate the second-order phase transition lines approaching a

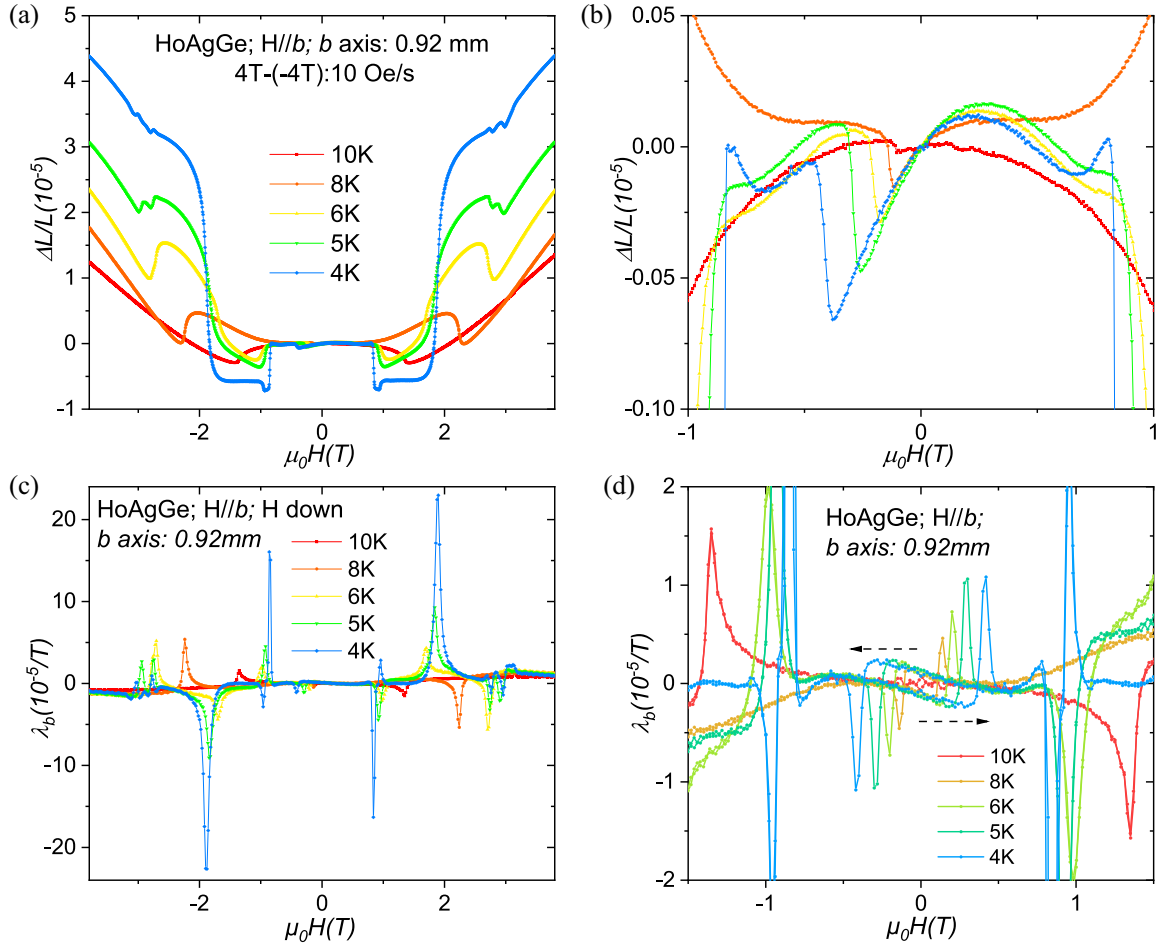

FIG. 7. Magnetostriction results of HoAgGe under H$\|b$. (a) Field-dependent relative length change $[\Delta L/L = [L(B) - L(0\ \mathrm{T})]/L(0\ \mathrm{T})]$ for HoAgGe along the b axis under H$\|b$ obtained upon the H decreasing condition at various temperatures, and the enlargement of the low field region in panel (b). (c) Field-dependent magnetostriction λ_b for HoAgGe along the b axis under H$\|b$ obtained upon the H decreasing condition at various temperatures. (d) Enlargement of the low field region of magnetostriction λ_b data with both the H increasing and decreasing conditions, with the increasing dataset obtained through antisymmetric operation of the H decreasing dataset in panel (d) on magnetic fields.

first-order one extending to low temperatures in the phase diagram of HoAgGe under H$\|b$ [see Fig. 2(f)], which has also been observed in CePdAl and YbAgGe [68,69]. The zoomed-in λ_b versus H curves in Fig. 7(d) give almost the same coercive fields as that from the $M(H)$, dM/dH, and ac susceptibility χ' curves [see Figs. 6(e), 6(f), and 12].

Taken together, the hysteretic behavior observed in both magnetization and magnetostriction data provides compelling evidence for the presence of TRS breaking in the zero-field, low-temperature phases of HoAgGe.

C. Nonlinear susceptibility in kagome spin ice

To see how nonlinear susceptibility arises in HoAgGe and related kagome spin ice models, we consider a general classical spin model with quadratic spin interactions subject to an external magnetic field:

$$H = \sum_{ij,\alpha\beta} J_{i\alpha,j\beta} n_{i\alpha} n_{j\beta} - g\mu_B S \sum_{i\alpha} B_\alpha n_{i\alpha}, \tag{8}$$

where spins are denoted by their length S multiplied by unit vectors $\hat{n}_i$. According to Eq. (5), $\chi^{(1)}$ is

$$\chi^{(1)}_{\alpha\beta\gamma} = (g\mu_B S)^3 \beta^2 \langle (\delta n^{\mathrm{tot}}_\alpha)(\delta n^{\mathrm{tot}}_\beta)(\delta n^{\mathrm{tot}}_\gamma)\rangle_0, \tag{9}$$

where $n^{\mathrm{tot}} \equiv \sum_i n_i$ and $\delta\hat{n}^{\mathrm{tot}} \equiv \hat{n}^{\mathrm{tot}} - \langle \hat{n}^{\mathrm{tot}}\rangle_0$.

To evaluate $\chi^{(1)}$, we recall that response properties of a symmetry-breaking state are determined by its elementary excitations. For general Ising spin systems where elementary excitations are single spin flips, the calculation of response functions for a particular symmetry breaking state should be done by tracing over excited states obtained from the given ground state by a relatively small number of spin flips, such as that considered in Ref [51]. For spin ice

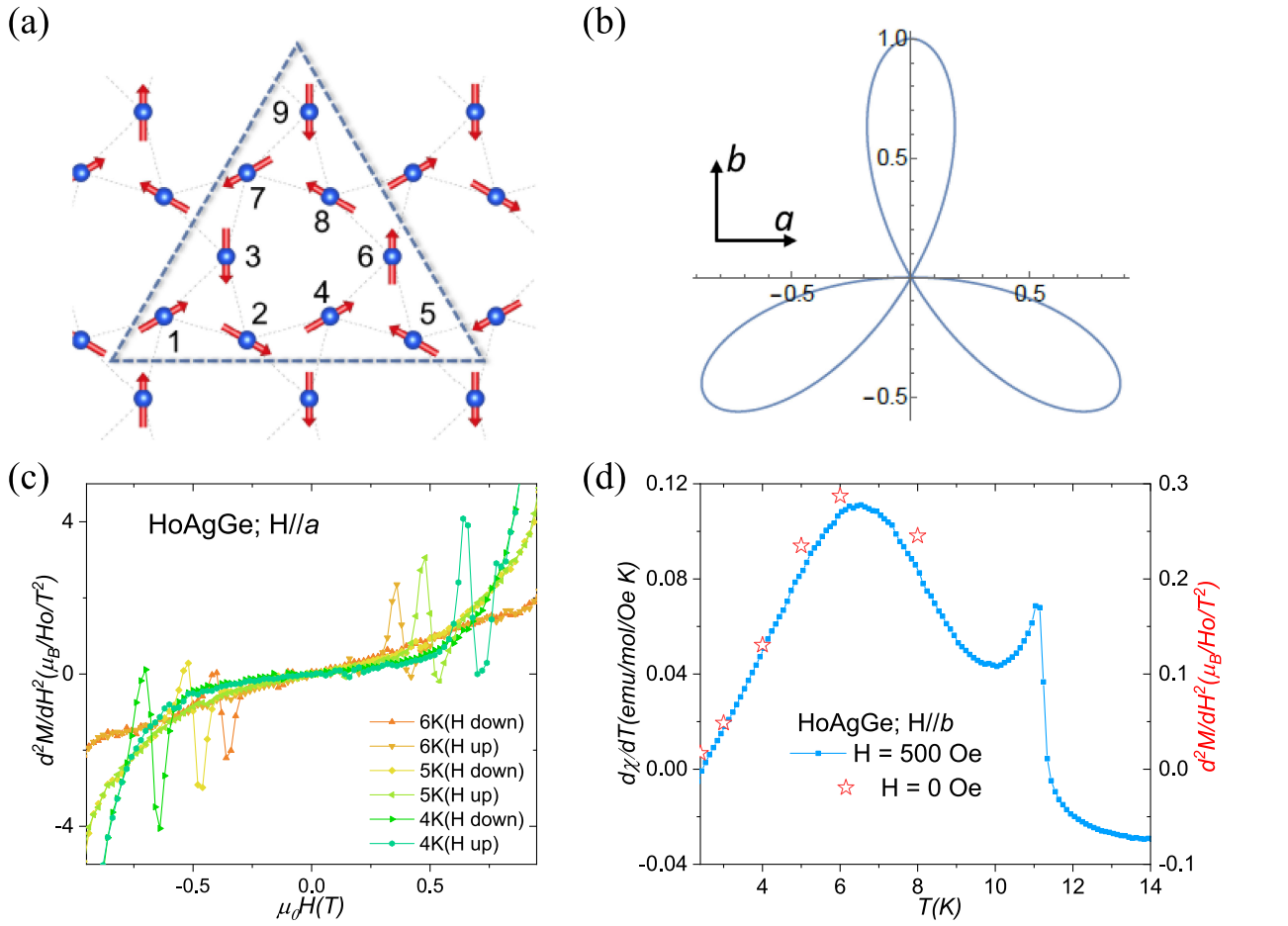

FIG. 8. Nonlinear magnetic susceptibility of HoAgGe. (a) Ground state $S_{\rm GS}$ of HoAgGe with only Ho spins shown. Labeled Ho spins enclosed in the dashed-line triangle belong to one magnetic unit cell; its TRS partner $S'_{\rm GS}$ could be obtained by flipping all nine Ho spins of $S_{\rm GS}$. The orientation of the local Ising axes for the three Ho sites in each triangle aligns with that in the ideal kagome lattice in panels (a) and (b). (b) Angular dependence of $\chi^{(1)}$ projected to the direction of a magnetic field rotating in the ab plane. The horizontal and vertical axes correspond to a and b axes as defined in Ref. [16]. (c) Enlargement of the low field region of d^2M/dH^2 data under H$\|a$ at various temperatures. (d) Left panel: low-temperature $d\chi/dT$ data of HoAgGe for H$\|b$ under 500 Oe; right panel: d^2M/dH^2 value with $\mu_0 H = 0$ T under H$\|b$ at various temperatures.

systems, it further requires the excited states to satisfy the ice rule.

For kagome spin ice, the difference between the ground state illustrated in Fig. 8(a) and its TRS partner already arises at the one-spin-flip level. To be concrete, in Table II, we list the net spin vector sum $\hat{n}^{\rm tot}$ for a total of six ice-rule excited states obtained by flipping a single Ho spin. One can see that $n_b^{\rm tot} = +2$ appears twice, but $n_b^{\rm tot} = -2$ appears zero times. In addition, $n_b^{\rm tot} = -1$ appears 4 times, but its time reversal $n_b^{\rm tot} = +1$ appears zero times. For the time-reversal partner of $S_{\rm GS}$, denoted by $S'_{\rm GS}$, all numbers in the right column of Table II just need to be multiplied by -1. Such an imbalance between time-reversal partners in the excited states is the reason for the nonvanishing $\chi^{(1)}_{bbb}$, as we show below.

To simplify the discussion, we assume all six one-spin-flip ice-rule states have the same energy E_1 relative to the ground-state energy. Ignoring all other excited states and considering the low-temperature limit, we have

$$\chi^{(1)}_{bbb} \approx (g\mu_B S)^3 \beta^2 e^{-\beta E_1} \sum_{1-\text{flip}} (n_b^{\rm tot})^3, \tag{10}$$

TABLE II. One-spin-flip ice-rule states from the ground state $S_{\rm GS}$ in Fig. 8(a) and the corresponding net spin vector.

Number of flipped spin	Net spin vector $(n_a^{\rm tot}, n_b^{\rm tot})$
1	$(-\sqrt{3}, -1)$
3	$(0, 2)$
4	$(-\sqrt{3}, -1)$
5	$(\sqrt{3}, -1)$
8	$(\sqrt{3}, -1)$
9	$(0, 2)$

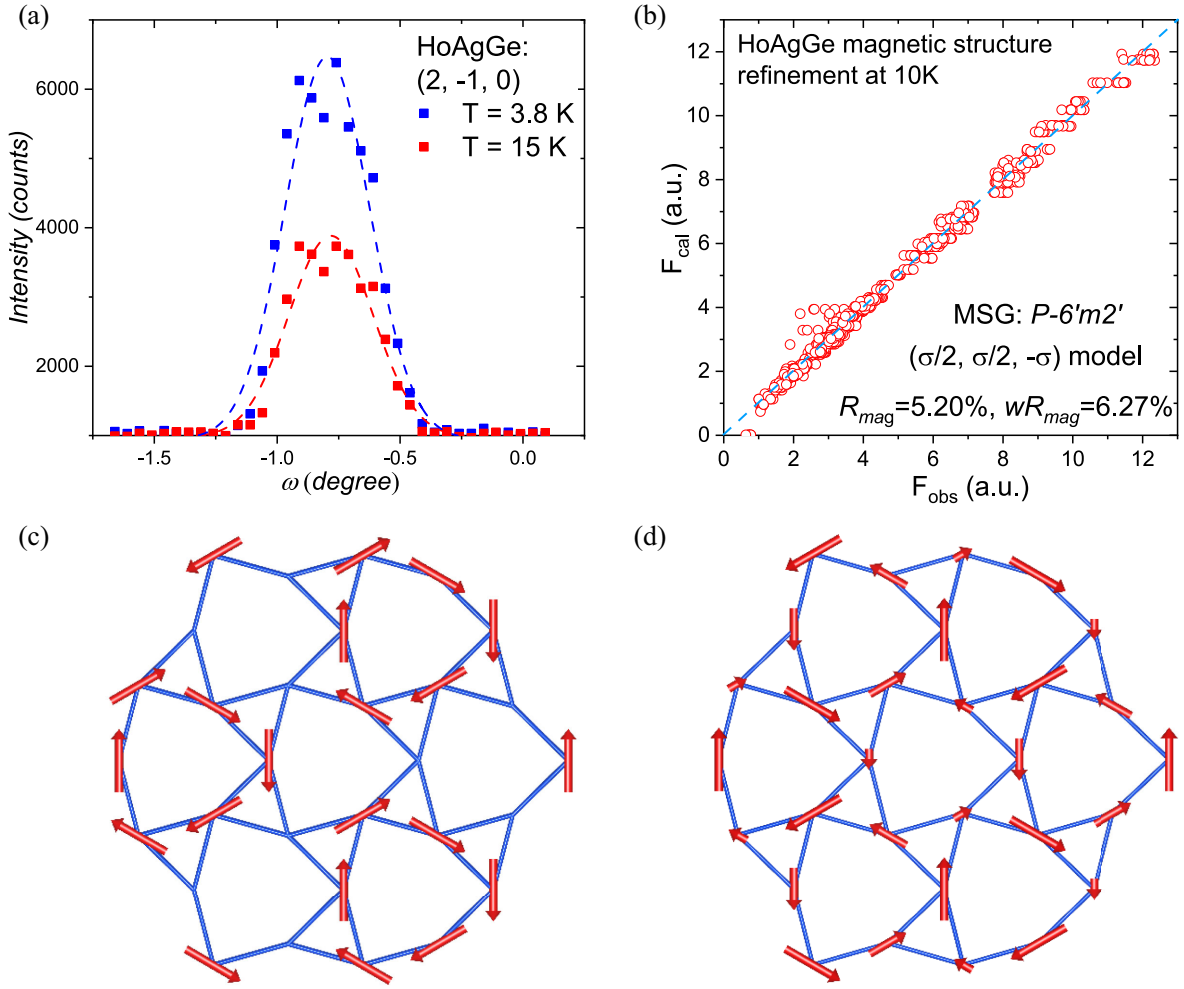

FIG. 9. (a) Rocking curves of nuclear site (2, −1, 0) of HoAgGe at 15 K and 3.8 K. (b) Plots of calculated vs experimental magnetic structure factors for the refined magnetic structure at 10 K with the $(\bar{\sigma}/2, \bar{\sigma}/2, -\bar{\sigma})$ model. Refined magnetic structures at 10 K with the $(\bar{\sigma}, -\bar{\sigma}, 0)$ (c) and $(\bar{\sigma}/3, 2\bar{\sigma}/3, -\bar{\sigma})$ (d) models.

where the sum is over all six one-spin-flip ice-rule states. Expressions of other components of $\chi^{(1)}$ can be written down in a similar manner. Using Table II, we obtain

$$\chi^{(1)}_{bbb} \approx 12(g\mu_B S)^3\beta^2 e^{-\beta E_1} \tag{11}$$

while $\chi^{(1)}_{aaa} = 0$. Clearly, repeating the calculation for S'_{GS} gives a negative $\chi^{(1)}_{bbb}$.

Using the 2D classical spin model and its parameters in Ref. [16], we find that $E_1 \approx 1.04$ meV. Note that this value is essentially the energy of the 1/3 plateau state relative to the ground state. At a temperature of 4 K, $\beta \sim 2.9$ meV^{-1} with $g\mu_B S \sim 0.58$ meV/T, we obtain $\chi^{(1)}_{bbb} \approx 1.85\ \mu_B\,\mathrm{T}^{-2}$ per Ho. If using the Ho moment size of $7.5\mu_B$ from neutron refinement instead of $10\mu_B$, we obtain $\chi^{(1)}_{bbb} \approx 0.78\ \mu_B\,\mathrm{T}^{-2}$. Moreover, the $\chi^{(1)}_b$ due to such spin-flip excitations is expected to vanish at 0 K (no excitations), and when T approaches T_2 from below ($\chi^{(1)}_b$ is forbidden by symmetry above T_2); hence, it is consistent with the experimental observation of its nonmonotonic temperature dependence.

IV. DISCUSSION AND CONCLUSION

Our work establishes that HoAgGe is a 3D stacked kagome spin ice with moderate interlayer ferromagnetic coupling. Its behavior, nonetheless, applies to general kagome ice physics as follows:

(1) The origin of $\chi^{(1)}$ in terms of ice-rule-compatible one-spin-flip excitations applies to generic kagome spin ice as well, thus standing as a genuine property of the TRS-breaking ground state of any variants of kagome spin ice sharing the same ground state.

(2) The rotational distortion of the kagome lattice in HoAgGe does not undermine the kagome ice properties. On an ideal kagome lattice, our 2D model (without J_c) corresponds to a J_1-J_2-J_3 model, i.e.,

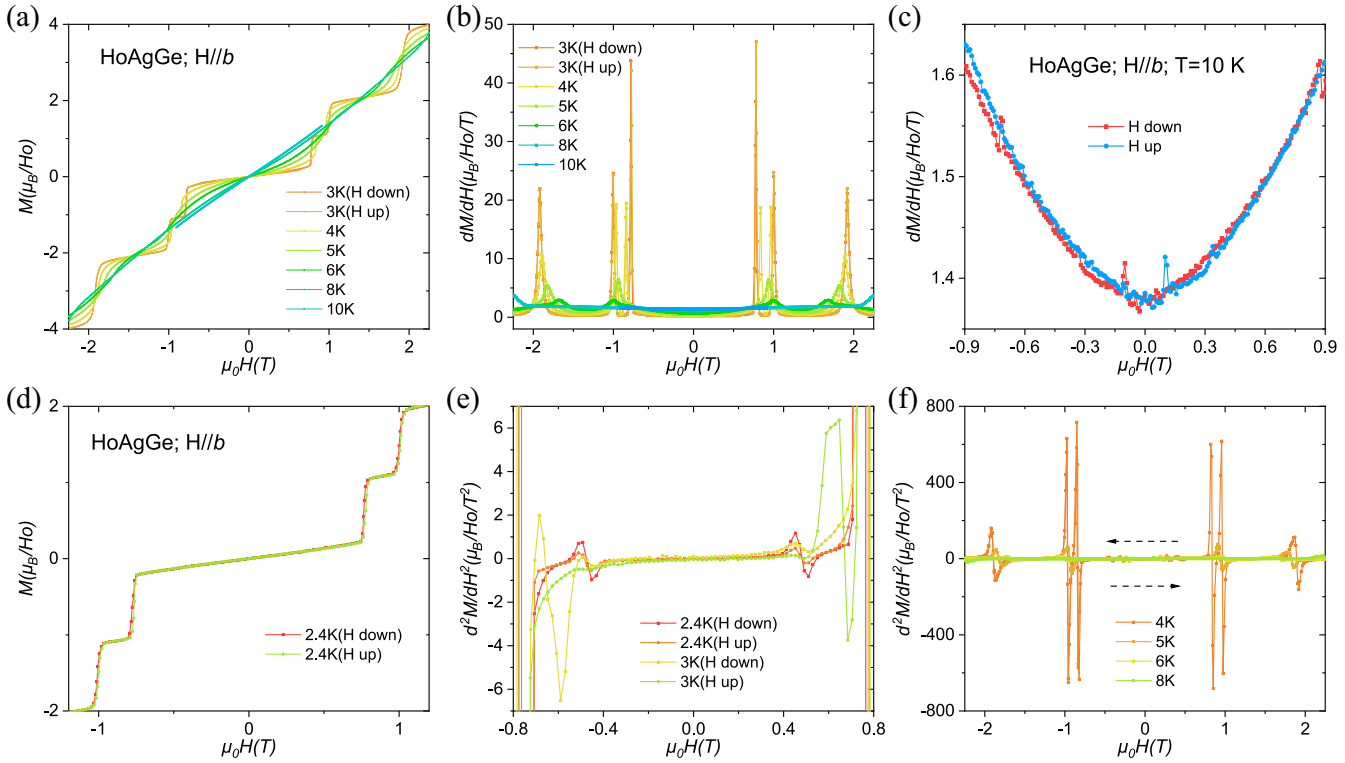

FIG. 10. Isothermal in-plane (H$\|b$) magnetization (a) and the corresponding differential susceptibility dM/dH for HoAgGe at various temperatures between 2.25 T and −2.25 T (b), at 10 K between 0.9 T and −0.9 T (c). Enlargement of the low field region of $M(H)$ data at 2.4 K (d) and d^2M/dH^2 data at various temperatures (e). And (f) the field dependence of d^2M/dH^2 data under H$\|b$ at various temperatures between 2.25 T and −2.25 T.

up to the third neighbor. The distortion splits the four second-nearest neighbors into two groups, respectively, coupled through J_2 and J_4 in our model. As already found in previous studies, the ordering behavior of kagome spin ice has certain robustness against changing the form of the spin Hamiltonian and parameter values, a common feature in critical phenomena. Particularizing to the 3D XY criticality revealed in this work, a minimal J_1-J_2-J_c kagome ice model is already sufficient to host the "divergence-free" KII phase. Our minimally extended models are therefore an indispensable link between the actual material HoAgGe and genuine kagome spin ice physics.

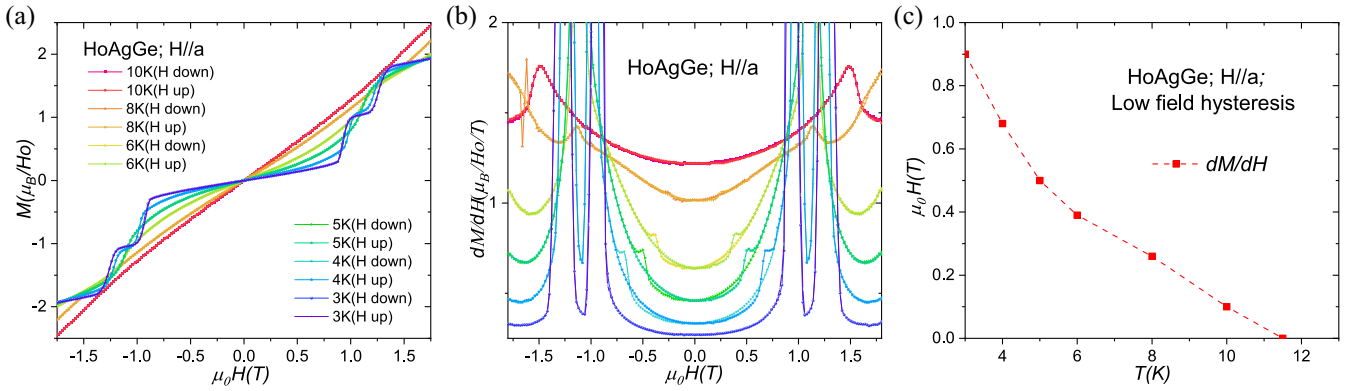

FIG. 11. Isothermal in-plane (H$\|a$) magnetization (a) and the corresponding differential susceptibility dM/dH (b) for HoAgGe at various temperatures. (c) Field and temperature dependence of low field hysteresis for HoAgGe under H$\|a$ as derived from $M(H)$ measurements.

(3) The critical behavior of HoAgGe is representative of 3D stacked kagome ice. Previous studies have established that the ordering pathways of kagome spin ice can be analyzed using a generalized six-state clock model [13–15,21,22] since the $\sqrt{3} \times \sqrt{3}$ ground state has exact sixfold degeneracy due to translation and time reversal. However, since HoAgGe is inherently 3D, it is expected to behave similarly to the 3D six-state clock model, which orders through a single 3D XY transition from the paramagnetic state [58,59]. As critical phenomena are inherently insensitive to material or model details and are predominantly determined by symmetry and dimension, we expect that our finding for HoAgGe applies to general quasi-2D kagome spin ice systems.

As far as we know, HoAgGe is the first spin system that exhibits a 3D XY criticality. Our work therefore adds a new member to the family of 3D XY universality, most famously represented by the superfluid transition of ^{4}He at 2.17 K [70–75]. Moreover, the critical behavior of HoAgGe is not the "trivial" 3D XY since it is known that anisotropic terms in 3D XY models are "dangerously irrelevant," which means that they are irrelevant in the renormalization group sense in the paramagnetic state but can change the critical behavior immediately below the transition in the ordered phase [60–64]. Such subtle behavior is indeed observed in our experiments as well as MC simulations, in that the critical exponents are difficult to obtain by fitting the data below T_2. For example, the magnetic (1/3, 1/3, 0) neutron peak can be used to extract the exponent β, which, for the 3D XY model, should be $\beta = 0.3485$. Using the peak intensity data very close to T_2 yields $\beta \sim 0.342(5)$ in Fig. 2(c), in good agreement with the 3D XY value. However, using the data between 9 K and 11.6 K [16] leads to different $\beta \sim 0.321(3)$. The dangerously irrelevant nature of the anisotropy term may also contribute to the slow ordering of the divergence channel below T_2 through a crossover.

Finally, we compare the ground state of HoAgGe to other popular metallic noncollinear AFM such as Mn_3X (X = Ir, Pt, Sn, Ge, etc.) and Mn_3NiN. In the latter, the TRS-breaking nature is reflected in their weak magnetization and the AHE, similar to that of ferromagnets [38–45], and they are, in this sense, "chiral." The ground state of HoAgGe [see Fig. 1(a)], and of kagome ice in general, belongs to a different category of chiral AFM, in the sense that the above "linear" properties as in typical ferromagnets vanish, but the two time-reversal partners still exhibit different nonlinear responses, allowing them to be distinguished and switched by external means. Such a functionality can potentially be exploited for information technology applications based on frustrated spin systems.

In summary, our work has established that HoAgGe is a 3D stacked kagome spin ice exhibiting 3D XY criticality and that it hosts a characteristic nonlinear magnetic susceptibility that allows its TRS-breaking partner states to be distinguished macroscopically. We expect our findings to inspire new theoretical developments for general kagome ice physics, such as exploring the effects of dimensionality, inversion symmetry breaking ($J_2 \neq J_4$), and new ways to probe and harness TRS-breaking phases in quantum spin systems.

ACKNOWLEDGMENTS

The authors would like to thank Vaclav Petříček, Oleg Tchernyshyov, Yuan Wan, Yoshi Tokiwa, Jianhui Xu, Zheng Deng, Xiancheng Wang, Jie Shen, Huifen Ren, and Shaokui Su for helpful discussions and experimental support. The work was supported by the National Key R&D Program of China (Grants No. 2023YFA1406003 and No. 2022YFA1402703), National Natural Science Foundation of China (Grants No. 12274015 and No. 12474139), the Beijing Natural Science Foundation (Grant No. JQ24012), and the Fundamental Research Funds for the Central Universities. The work in Augsburg was supported by the German Research Foundation (DFG) through TRR360 (Project No. 492547816). H. C. acknowledges support by NSF Awards No. DMR-1945023 and No. DMR-2531960. The instrument POLI at Heinz Maier-Leibnitz Zentrum (MLZ), Garching, Germany, was operated by RWTH Aachen University in cooperation with FZ Jülich (Jülich Aachen Research Alliance JARA). We are grateful to the extreme condition characterization platform of the Analysis & Testing Center of Beihang University for the facilities and the scientific and technical assistance. A portion of this work was conducted at the Synergetic Extreme Condition User Facility (SECUF).

K. Z. and P. G. proposed the experiments; K. Z., J. S. G., and X. L. C. synthesized single crystals and conducted specific heat measurements; K. Z. and N. O. conducted magnetostriction measurements; K. Z. and C. Q. J. performed magnetometry measurements; H. D. and V. H. conducted single-crystal elastic neutron scattering; H. D., T. M., Y. X. S., and M. J. G. measured single-crystal diffuse neutron scattering; N. S. M. and C. T. performed MC simulations and scaling analysis; H. C. proposed ternary plot representation and provided nonlinear susceptibility calculations; K. Z., H. C., and P. G. wrote the manuscript with input from all authors.

DATA AVAILABILITY

The data that support the findings of this article are not publicly available upon publication because it is not technically feasible and/or the cost of preparing, depositing, and hosting the data would be prohibitive within the terms of this research project. The data are available from the authors upon reasonable request.

APPENDIX A: METHODS

1. Single-crystal growth and characterization

High-quality single crystals of HoAgGe were grown using the Ag–Ge-rich self-flux method, with typical concentration $R_{0.06}(Ag_{0.75}Ge_{0.25})_{0.94}$ (R: Ho and Lu) [76]. Mixtures were placed in alumina crucibles and sealed in a quartz tube, heated to 1150 °C, held there for 10 h and cooled to 836 °C within 76 h, where the flux was decanted using a centrifuge. All single crystals were characterized via x-ray diffraction with a Laue backscattering diffractometer using Cu $K\alpha$ radiation.

2. Magnetic and thermodynamic measurements, and demagnetization correction

Magnetization measurements were performed using a vibrating sample magnetometer (Quantum Design MPMS). The specific heat data were obtained with Quantum Design PPMS. The magnetostriction measurement along the b axis of HoAgGe under the H$\|b$ axis was measured by utilizing a high-resolution capacitive dilatometer in the PPMS [77,78]. The demagnetization correction was considered for the magnetic and thermodynamic measurements, according to the different shapes of HoAgGe crystals [79].

3. Elastic neutron scattering and magnetic structure refinement

Elastic neutron scattering experiments were conducted on the short-wavelength single-crystal diffractometer POLI at Maier-Leibnitz Zentrum (MLZ) Germany using nonpolarized neutrons [80,81]; the technical details can be found in the Supplemental Material of Ref. [16]. The magnetic structures were determined using Jana 2006 software [82–84].

4. Diffuse neutron scattering of HoAgGe single crystal

The diffuse scattering experiment was performed on the DNS spectrometer at MLZ on coaligned HoAgGe single crystals to probe the elastic spin correlations with polarized neutrons [85]. To avoid unexpected incoherent scattering from commonly used varnish, the crystals were fixed on the flat copper plates using hydrogen-free varnish and then fixed on a copper holder. The neutron wavelength adopted for the experiment was 4.74 Å.

The elastic neutron scattering experiment of HoAgGe at 15 K was conducted on the time-of-flight single-crystal diffractometer SXD at ISIS, UK using nonpolarized neutrons, with the intensity normalized with vanadium measurement [86].

5. Monte Carlo simulation

In this work, all computational results for the two- and three-dimensional classical Ising models were obtained using classical MC simulations based on the Metropolis algorithm [87] with periodic boundary conditions. At each MC step, a single spin was randomly selected and flipped. The flip was accepted according to the Metropolis criterion $P_{\text{accept}} = \min(1, e^{-\beta\Delta E})$ with P_{accept} the flipping probability, β the inverse of temperature, and ΔE the energy difference between before and after flipping. Each Monte Carlo sweep consisted of N such spin-flip attempts, where N is the total number of spins in the lattice.

To ensure equilibration, the system was first evolved for 10^4–2×10^4 MC sweeps, with the exact number depending on the system size [88]. Physical observables—including the order parameter M and the specific heat—were measured after equilibration. The measurements were averaged over an additional 2 times the equilibration sweep to ensure the statistical accuracy.

APPENDIX B: MAGNETIC STRUCTURE REFINEMENT AND THE LOW-TEMPERATURE MAGNETIC PROPERTY, INCLUDING *ac* SUSCEPTIBILITY OF HoAgGe SINGLE CRYSTALS

The low-temperature dc susceptibilities $\chi(T)$ of HoAgGe were measured for H$\|b$ under 500 Oe, 2000 Oe, and 3000 Oe, respectively. The two transitions, labeled

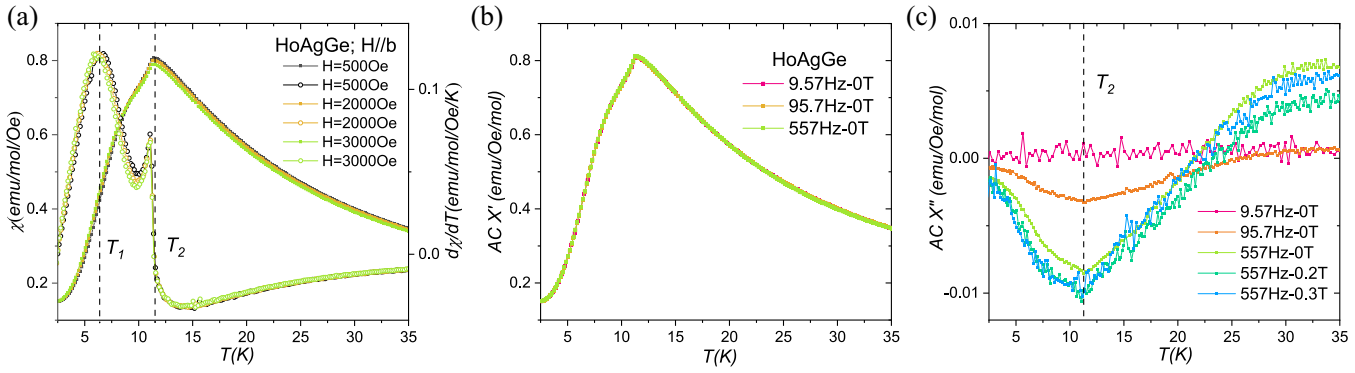

FIG. 12. (a) Low-temperature susceptibility $\chi(T)$ of HoAgGe for H$\|b$ under 500 Oe, 2000 Oe, and 3000 Oe, with $d\chi(T)/dT$ in the right panel. (b) The ac susceptibility $\chi'(T)$ of HoAgGe with 9.57 Hz, 95.7 Hz and 557 Hz, respectively. (c) The ac susceptibility $\chi''(T)$ with various frequencies and fields along the b axis, respectively.

$T_1 \sim 7$ K and $T_2 = 11.6$ K, can be clearly observed in Fig. 12(a) and exhibit a slight shift toward lower temperatures with increasing magnetic field up to 3000 Oe. As shown in Fig. 12(b), the ac susceptibility $\chi'(T)$ curve of HoAgGe measured at frequencies of 9.57 Hz, 95.7 Hz, and 557 Hz is identical to the $\chi(T)$ data obtained under $H_b = 500$ Oe in Fig. 12(a).

At a fixed frequency of 557 Hz, the $\chi'(T)$ curves exhibit a clear difference below T_2 as the magnetic field along the b axis increases. Upon entering the magnetic space group P-6′m2′, an additional peak feature emerges in the $d\chi'(T)/dT$ curve, superimposed on the broad anomaly centered at $T_1 \sim 7$ K, occurring at 5.9 K and 4.7 K under $H_b = 0.2$ T and 0.3 T, respectively. Notably, this behavior is absent in the dc susceptibility data shown in Fig. 12(a), indicating the dynamic origin of the nonlinear response in the kagome spin ice state.

As shown in the phase diagram in Fig. 6(f), the data points extracted from the $\chi'(T)$ curves exhibit good consistency with the datasets derived from $M(H)$ and λ_b measurements. Furthermore, as the frequency increases, the imaginary part of the ac susceptibility $\chi''(T)$ in Fig. 12(c) exhibits an anomaly at $T_2 = 11.6$ K. Meanwhile, the noise level in the $\chi''(T)$ curve increases with increasing applied magnetic field.

APPENDIX C: DIFFUSE SCATTERING OF HoAgGe SINGLE CRYSTAL WITH POLARIZED AND UNPOLARIZED NEUTRONS

The experiment setup at the DNS station is briefly listed in Fig. 13(a), with the coaligned single crystals fixed as the c axis along the vertical direction in Fig. 13(b), to detect the (HK0) scattering plane. The conventional polarization configurations used for standard experiments were set to $\boldsymbol{P}\|\mathrm{z}\perp\boldsymbol{Q}$, with $\boldsymbol{P}$ the polarization direction and $\boldsymbol{Q}$ the neutron momentum transfer.

Concerning polarized neutron diffuse scattering at the DNS station, as shown in Figs. 1(e) and 1(f), the green circle close to the second Brillouin zone (BZ) boundary is due to the background signal during the measurement. Note the powder ring of (2, 2, 0) diffraction from the Cu plate

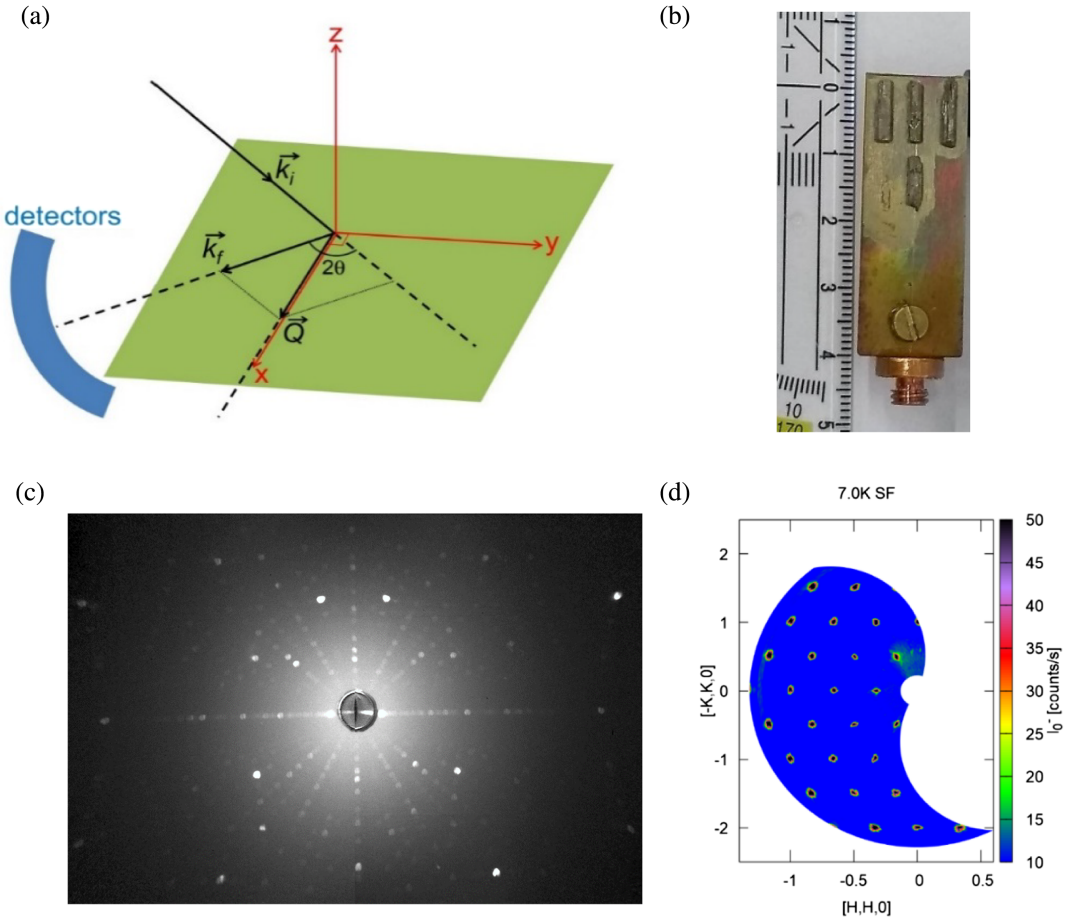

FIG. 13. (a) Illustration of the polarized neutron diffuse scattering process of the HoAgGe single crystal at SXD station. (b) Optical image of four coaligned HoAgGe single crystals used for the neutron diffuse and INS measurement, fixed on a copper holder. (c) Laue image of a HoAgGe single crystal shown above with the horizontal direction being the (100) orientation and the vertical direction being the (001) orientation. (d) SF channel of diffuse scattering at 7 K.

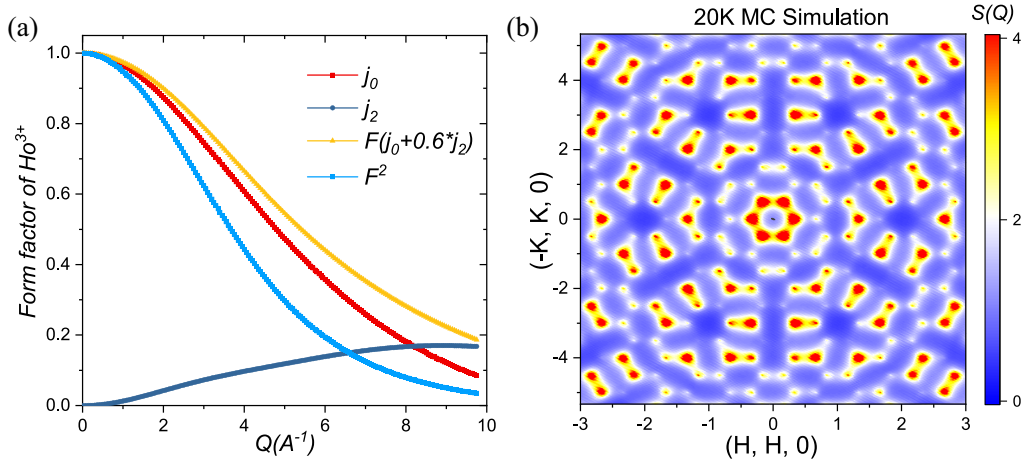

FIG. 14. (a) Q dependence of magnetic form factor $F(q)$ of the Ho^{3+} ion. (b) Magnetic structure factor $S(Q)$ for the kagome ice I state at $T = 20$ K within the large q space.

in Fig. 13(b). Its d value 1.28 $Å^{-1}$ is slight larger than 1.18 $Å^{-1}$ of magnetic diffraction $(-2/3, -2/3, 0)$, consistent with the cases in Figs. 1(e) and 1(f).

Intriguingly, the short-range spin ice correlations have been detected not only in the (H, K, 0) plane but also in the (H, K, 1), (H, K, 2), and (H, K, 3) planes, respectively. With L changing from 0 to 3, the diffuse scattering pattern is the combination of spin ice correlation due to the magnetic exchange interaction between Ho^{3+} ions, together with the magnetic form factor F of

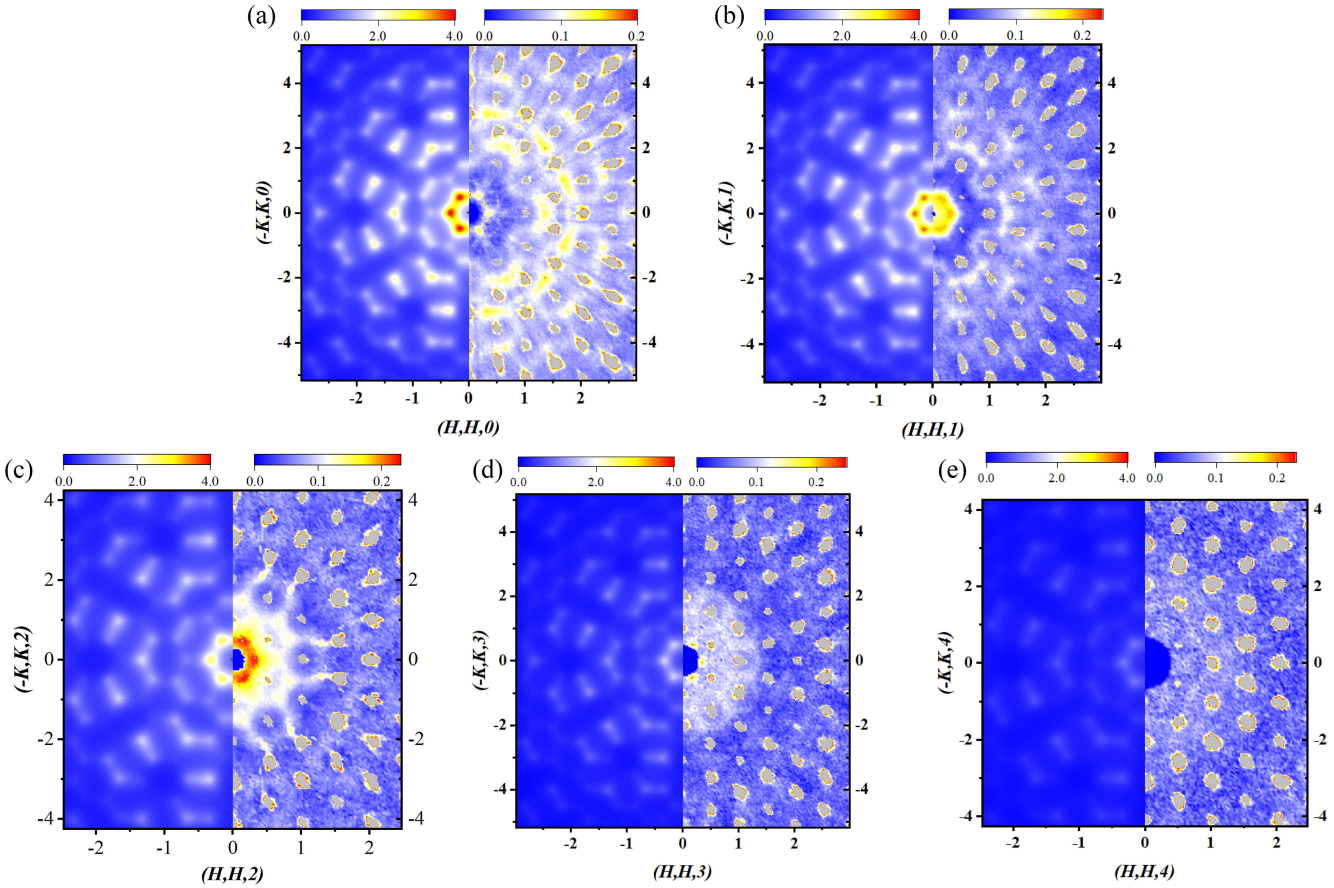

FIG. 15. (a)–(e) Diffuse neutron scattering pattern of the HoAgGe single crystal at 15 K at the SXD station within the (H, K, L) ($L = 0$, 1, 2, 3, and 4) plane (right panel), together with the simulated diffuse scattering pattern at 20 K (left panel).

the Ho^{3+} ion, which could be expressed as

$$F = j_0(q) + \frac{2-g}{g} j_2(q),$$

with the g factor being 1.25 for Ho^{3+}; $j_0(q)$, $j_2(q)$, and $F(q)$ could be found in Fig. 14(a). The spin ice correlations are clearly demonstrated at 20 K in Fig. 14(b) based on the 3D kagome spin ice model (see below) within a large q value. Here, we focus on the influence of the magnetic form factor on the diffuse scattering spectra.

As shown in Figs. 15(a)–15(e), the left panel is the theoretical simulation pattern, accounting for the $F(q)$ influence, with the right panel the diffuse pattern of HoAgGe at the SXD station at 15 K. For the $L = 0$ and 1 cases, the diffuse scattering spectra are basically similar to the simulated pattern. The unique variations of the scattering pattern within the (H, K, L) ($L = 2$ and 3) plane are mainly due to the $F(q)$ effect, together with the polarization factor issue. Note the neutron dipole moment only interacts with the spin component perpendicular to the scattering vector $\boldsymbol{q}$. Thus, for kagome spin ice orders in the ab plane, the polarization factor might change considerably for the scattering vector $\boldsymbol{q}$ in the large L plane. In addition, the diffuse scattering is almost invisible due to the large q value at the (H, K, 4) plane, with $q > 6$ Å^{-1} and $I = F^2 < 0.2$.

APPENDIX D: THE 3D KAGOME SPIN ICE MODEL FOR HoAgGe

Adding the ferromagnetic nearest-neighbor interlayer coupling J_c, the 3D spin model would go through a single 3D XY phase transition into the ground state. Correspondingly, both the order parameter M and the magnetic charge per triangle Q start to increase below $T_2 = 17.8$ K in Figs. 16(a) and 16(b).

Regarding the upper limit of J_c, Fig. 16(c) summarizes the Monte Carlo simulated specific heat C_{mag} curves based on the 3D spin model with $J_c = 0.9$ meV for various lattice sizes. For a lattice size of $18 \times 18 \times 18$, the C_{mag} curve exhibits two magnetic transitions: a sharp peak at $T_2 = 27.5$ K and a broader anomaly centered at $T_1 = 12.4$ K, which is significantly higher than the experimental value observed in HoAgGe. Therefore, J_c should lie within the range $0.45 * J_1 > J_c > J_2$ in the 3D model that includes both the magnetic interactions J_1-J_4 and the dipolar interaction E_d.

In the MC simulation of thermodynamic properties and scaling analyses, we used 3D kagome lattices of size $L \times L \times L$, while in the calculation of order parameter M, we chose the results of a single two-dimensional kagome layer. The spin order should be the same for each kagome layer connected by the ferromagnetic interlayer interactions, which is the case in our simulation. Additionally, this choice can also avoid the possible fluctuation caused by the finite-size effect between different layers as the temperature increases if only a single layer is chosen. Thus, the value of M averaged over all the MC simulation samples can be regarded as the order parameter for the whole system.

APPENDIX E: TERNARY PLOT REPRESENTATION OF INTERMEDIATE ORDER

We first discuss what the vanishing magnetic contributions at nuclear sites of the elastic neutron scattering intensities mean. For the hexagonal lattice of HoAgGe, if we choose the primitive Bravais lattice vectors as

$$\mathbf{a}_1 = a\hat{x}, \qquad \mathbf{a}_2 = -\frac{a}{2}\hat{x} + \frac{\sqrt{3}a}{2}\hat{y}, \qquad \mathbf{a}_3 = c\hat{z},$$

where $a = 7.0862$ Å and $b = 4.186$ Å, we have the reciprocal lattice vectors

$$\mathbf{b}_1 = \frac{4\pi}{\sqrt{3}a}\left(\frac{\sqrt{3}}{2}\hat{x} + \frac{1}{2}\hat{y}\right), \qquad \mathbf{b}_2 = \frac{4\pi}{\sqrt{3}a}\hat{y}, \qquad \mathbf{b}_3 = \frac{2\pi}{c}\hat{z}.$$

Below T_2 and at zero magnetic field, the unit cell is tripled because of magnetic ordering. The magnetic unit

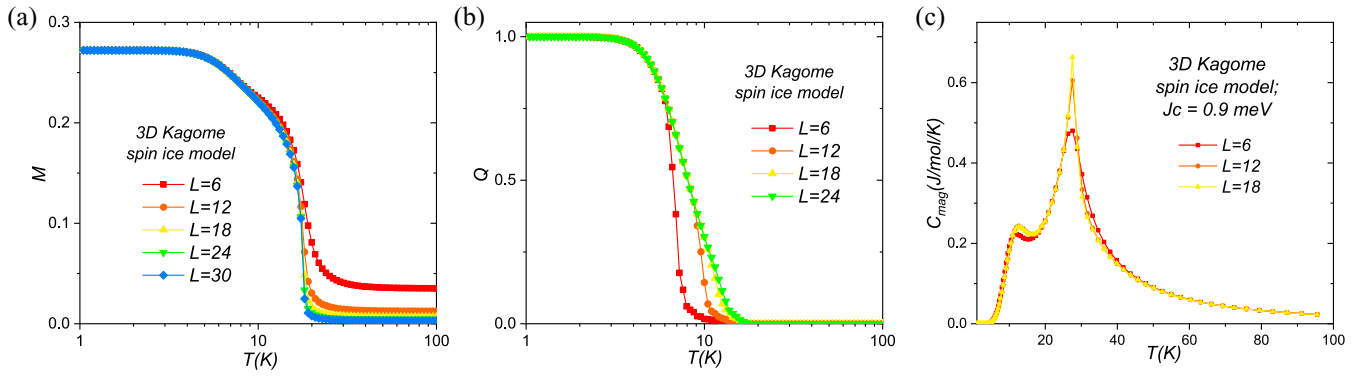

FIG. 16. Monte Carlo simulated (a) complex-order parameter M and (b) magnetic charge per triangle Q, and (c) magnetic specific heat C_{mag} based on the 3D spin model with various lattice sizes (see text).

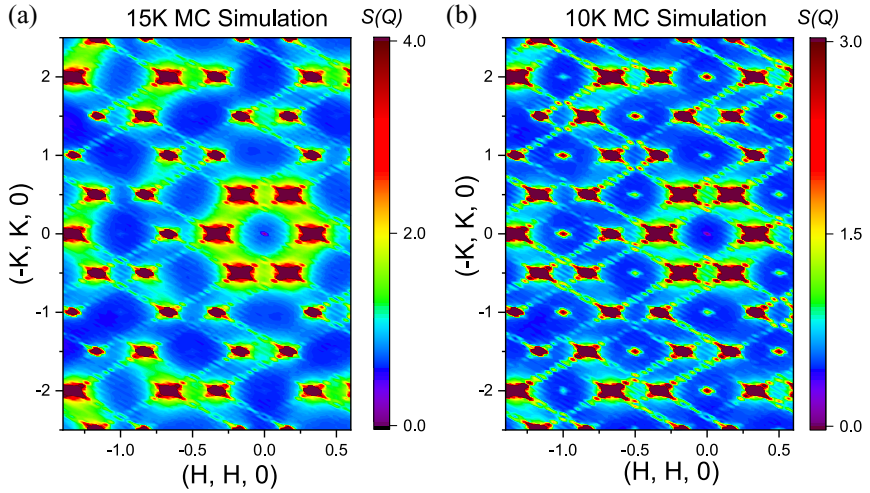

FIG. 17. Magnetic structure factor $S(Q)$ from MC simulations based on the 3D spin model at (a) $T = 15$ K and (b) $T = 10$ K, respectively.

cells have primitive lattice vectors

$$\mathbf{a}_1^M = 2\mathbf{a}_1 + \mathbf{a}_2, \qquad \mathbf{a}_2^M = 2\mathbf{a}_2 + \mathbf{a}_1, \qquad \mathbf{a}_3^M = \mathbf{a}_3.$$

The corresponding reciprocal lattice vectors are

$$\mathbf{b}_1^M = \frac{4\pi}{3a}\hat{x}, \qquad \mathbf{b}_2^M = \frac{4\pi}{3a}\left(-\frac{1}{2}\hat{x} + \frac{\sqrt{3}}{2}\hat{y}\right), \qquad \mathbf{b}_3^M = \frac{2\pi}{c}\hat{z}.$$

We assume that a general spin in the structural unit cell labeled by i and a sublattice labeled by α is denoted by

$$\mathbf{S}_{i\alpha} = \sigma_{i\alpha}\hat{n}_\alpha$$

where $\hat{n}_\alpha$ is a unit vector along the local Ising axis on sublattice α and $\sigma_{i\alpha} = \pm 1$ is an Ising variable. For simplicity, we only consider the static structure factor due to the σ variables on the same sublattices,

$$S_{\mathbf{q}} = \frac{1}{N}\sum_{ij,\alpha}\langle\sigma_{i\alpha}\sigma_{j\alpha}\rangle e^{i(\mathbf{R}_j - \mathbf{R}_i)\cdot\mathbf{q}}.$$

Because of the magnetic ordering, peaks of $S_{\mathbf{q}}$ will generally appear at $\mathbf{q} = \mathbf{q}^M = q_1\mathbf{b}_1^M + q_2\mathbf{b}_2^M + q_3\mathbf{b}_3^M$, where $q_{1,2,3}$ are integers. Namely,

$$S_{\mathbf{q}^M} = \frac{1}{N}\sum_{ij,\alpha}\langle\sigma_{i\alpha}\sigma_{j\alpha}\rangle e^{i(\mathbf{R}_j - \mathbf{R}_i)\cdot\mathbf{q}} \propto N.$$

If, however, certain $S_{\mathbf{q}^M} = 0$, we need

$$\begin{aligned}&\frac{1}{N}\sum_{ij,\alpha}\langle\sigma_{i\alpha}\sigma_{j\alpha}\rangle e^{i(\mathbf{R}_j - \mathbf{R}_i)\cdot\mathbf{q}}\\ &\approx \frac{N}{9}\sum_{i\alpha\in\text{muc}}\sum_{\mathbf{R}_j - \mathbf{R}_i\in\text{ws}}\frac{1}{d_{ij}}\bar{\sigma}_{i\alpha}\bar{\sigma}_{j\alpha}e^{(\mathbf{R}_j - \mathbf{R}_i)\cdot\mathbf{q}^M}\\ &= 0\end{aligned} \tag{D1}$$

where the first sum is over all sites within a magnetic unit cell, the second sum is over all j such that the vector $\mathbf{R}_j - \mathbf{R}_i$ does not go beyond the first Wigner-Seitz magnetic unit cell, and d_{ij} is a degeneracy factor accounting for the number of Wigner-Seitz cells sharing the same site $j\alpha$. The approximation amounts to replacing all $\sigma_{i\alpha} = \bar{\sigma}_{i\alpha} + \delta\sigma_{i\alpha}$ by their ordered parts $\bar{\sigma}_{i\alpha}$.

We next see what Eq. (D1) translates to for the present system. We pick the magnetic unit cell by combining the original unit cell and its translation by $\mathbf{a}_1$ and $\mathbf{a}_1 + \mathbf{a}_2$, respectively, as depicted by the solid triangle in Fig. 8(a). We label the three sublattices in the original unit cell counterclockwise starting from the bottom-left corner as $\alpha = 1, 2, 3$, and the three unit cells in the magnetic unit cell as $A = 1, 2, 3$, also counterclockwise from the bottom-left corner. The nine spins in the magnetic unit cell are therefore denoted by $\sigma_{\alpha Aj}$, where j labels magnetic unit cells. Their positions are at

$$\mathbf{r}_{\alpha Aj} = \mathbf{R}_j^M + \boldsymbol{\tau}_\alpha + \boldsymbol{\pi}_A$$

where $\mathbf{R}_j^M$ are magnetic lattice vectors, $\boldsymbol{\tau}_\alpha$ are the positions of the sublattices in the structural unit cell, and

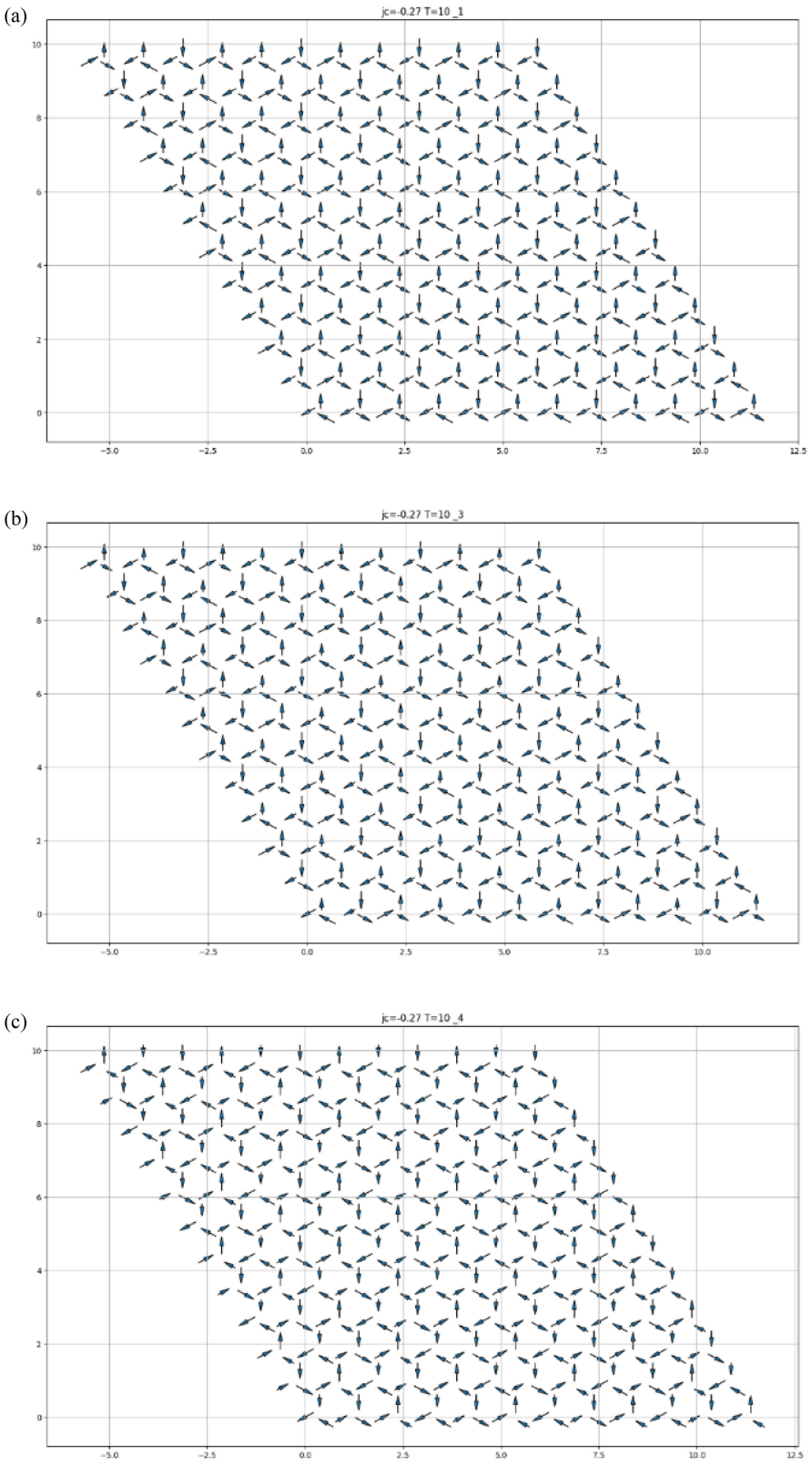

Fig. 18. (Continued).

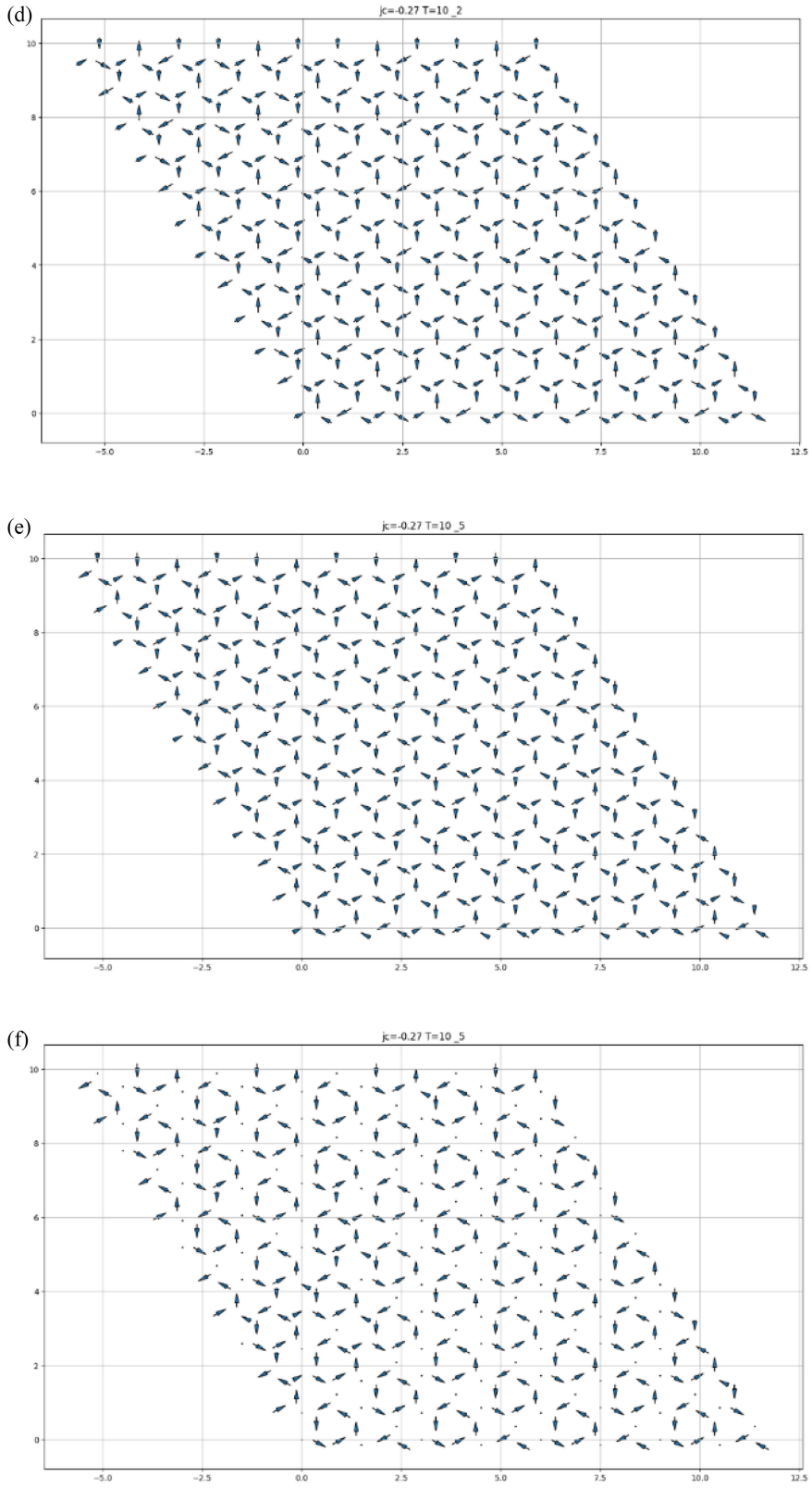

FIG. 18. (a)–(f) Averaged spin configurations within the single kagome layer from the Monte Carlo simulations in a 12×12 unit cell at $T = 10$ K, with the arrow length indicating the order moment size of the Ho spin.

$$\boldsymbol{\pi}_1 = 0, \qquad \boldsymbol{\pi}_2 = \mathbf{a}_1, \qquad \boldsymbol{\pi}_3 = \mathbf{a}_1 + \mathbf{a}_2$$

Then,

$$S_{\mathbf{q}^M} \approx \frac{N}{9} \sum_{A\alpha} \sum_{ws} \frac{1}{d_{0A,jB}} \bar{\sigma}_{0A\alpha} \bar{\sigma}_{jB\alpha} e^{i(\mathbf{R}_j^M + \boldsymbol{\pi}_B - \boldsymbol{\pi}_A)\cdot \mathbf{q}^M}$$

where the second sum is over jB, which satisfies $\mathbf{R}_j^M + \boldsymbol{\pi}_B - \boldsymbol{\pi}_A \in \mathrm{ws}$. This case is nothing but the six nearest neighbors of $\bar{\sigma}_{0A\alpha}$ on the same structural sublattices, each having $d_{0A,jB} = 3$, plus site $0A$ itself. We thus have

$$S_{\mathbf{q}^M} \approx \frac{N}{9} \sum_{\alpha} \left\{ \frac{2}{3} \mathrm{Re}[e^{i\mathbf{a}_1\cdot\mathbf{q}^M} + e^{i\mathbf{a}_2\cdot\mathbf{q}^M} + e^{-i(\mathbf{a}_1+\mathbf{a}_2)\cdot\mathbf{q}^M}] \times (\bar{\sigma}_{1\alpha}\bar{\sigma}_{2\alpha} + \bar{\sigma}_{2\alpha}\bar{\sigma}_{3\alpha} + \bar{\sigma}_{3\alpha}\bar{\sigma}_{1\alpha}) + (\bar{\sigma}_{1\alpha}^2 + \bar{\sigma}_{2\alpha}^2 + \bar{\sigma}_{3\alpha}^2) \right\}.$$

In the present case, $S_{\mathbf{q}^M}$ vanishes for any $\mathbf{q}^M = q_1\mathbf{b}_1 + q_2\mathbf{b}_2 + q_3\mathbf{b}_3$, i.e., the structural reciprocal lattice vectors, which results in

$$\begin{aligned} 0 = S_{\mathbf{q}^M} &\approx \frac{N}{9}(2\bar{\sigma}_{1\alpha}\bar{\sigma}_{2\alpha} + 2\bar{\sigma}_{2\alpha}\bar{\sigma}_{3\alpha} + 2\bar{\sigma}_{3\alpha}\bar{\sigma}_{1\alpha} + \bar{\sigma}_{1\alpha}^2 \\ &\quad + \bar{\sigma}_{2\alpha}^2 + \bar{\sigma}_{3\alpha}^2) \\ &= \frac{N}{9}\sum_{\alpha}(\bar{\sigma}_{1\alpha} + \bar{\sigma}_{2\alpha} + \bar{\sigma}_{3\alpha})^2. \end{aligned} \tag{D2}$$

Namely, the intermediate phase must satisfy the constraint that the Ising spins on the same structural sublattice in the magnetic unit cell sum to zero. Additionally, the kagome ice rule dictates that

$$\sigma_{jA1} + \sigma_{jA2} + \sigma_{jA3} \equiv Q_{jA} = \pm 1 \tag{D3}$$

where Q_{jA} is the magnetic charge on plaquette jA, which constrains the fluctuating $\sigma_{jA\alpha}$ but not the ordered part $\bar{\sigma}_{jA\alpha}$ individually. Two common situations considered in previous works are the charge-ordered phase, which amounts to $\bar{Q}_{jA} = \pm 1$ but $\bar{\sigma}_{jA\alpha} = 0$, and the partial-ordered phase, which corresponds to $\bar{Q}_{jA} = 0$ and $(\bar{\sigma}_{jA1}, \bar{\sigma}_{jA2}, \bar{\sigma}_{jA3}) = (0,1,-1), (1,0,-1), \ldots$. Both cases also satisfy the constraint for the intermediate phase, Eq. (D3), but the charge-ordered phase does not have Bragg peaks since $\bar{\sigma}_{jA\alpha} = 0$. Therefore, only the partial-ordered phase was considered in Refs. [16] and [17]. However, there are other possible phases that satisfy both Eqs. (D2) and (D3). Our goal is to find a suitable quantity that can compactly represent such orderings and their degeneracies.

To this end, we first look into the complex-order parameter in the main text:

$$M = \frac{1}{N}\sum_i \sigma_i e^{i\mathbf{Q}\cdot\mathbf{r}_i} \tag{D4}$$

where $\mathbf{Q} = [(4\pi)/(3a)]\hat{x} = \mathbf{b}_1^M$ and N is the total number of spins (while our N above is the total number of unit cells). In our notation,

$$M = \bar{M} = \frac{1}{9}\sum_{A\alpha} \bar{\alpha}_{A\alpha} e^{i\mathbf{b}_1^M\cdot(\tau_\alpha + \pi_A)}.$$

For the partial-ordered phase, we have

$$\begin{aligned} (\bar{\sigma}_{11}, \bar{\sigma}_{12}, \bar{\sigma}_{13}) &= (\bar{\sigma}_{22}, \bar{\sigma}_{23}, \bar{\sigma}_{21}) \\ &= (\bar{\sigma}_{33}, \bar{\sigma}_{31}, \bar{\sigma}_{32}) \equiv (\sigma_1, \sigma_2, \sigma_3) \\ &= (0,-1,1), (1,-1,0), (1,0,-1), \\ &\quad (0,1,-1), (-1,1,0), (-1,0,1) \end{aligned} \tag{D5}$$

where the first line is a requirement of C_3 symmetry. The second line can be viewed as all permutations of $(1,-1,0)$. If we only consider possible phases that satisfy the first line of Eq. (D5), M becomes (here, we do not consider the distortion of the kagome lattice)

$$M = \frac{2}{9}(\sigma_1 + e^{i\frac{2\pi}{3}}\sigma_2 + e^{i\frac{4\pi}{3}}\sigma_3)$$

As a result, any cyclic permutation of $\sigma_{1,2,3}$ is equivalent to multiplying M by $e^{i\frac{2\pi}{3}}$ or $e^{i\frac{4\pi}{3}}$, while the anticyclic permutations can be obtained from the former by complex conjugation. Therefore, M will be located at six vertices of a hexagon centered at the origin on the complex plane.

Since the intermediate phase supposedly only depends on two free parameters ($\sigma_{1,2,3}$ with the constraint $\sigma_1 + \sigma_2 + \sigma_3$), and M as a complex number has two independent degrees of freedom, the latter can, in principle, describe any possible intermediate phases. However, when M from MC simulations falls onto a ring, which is due to the prevalence of domains, it is more desirable to understand what spin structures each domain has. Then, such structures are mostly likely the symmetry-breaking states in the actual 3D material. However, M is not ideally suited for such a purpose since it is defined as a summation over the whole system. Instead, it is more desirable to use $\sigma_{1,2,3}$ directly, which can be plotted in real space.

We therefore propose to use the triad

$$(\sigma_1, \sigma_2, \sigma_3)_j = \left(\frac{\sigma_{j11} + \sigma_{j22} + \sigma_{j33}}{3}, \frac{\sigma_{j12} + \sigma_{j23} + \sigma_{j31}}{3}, \frac{\sigma_{j13} + \sigma_{j21} + \sigma_{j32}}{3} \right) - \frac{1}{9}\sum_{A\alpha} \sigma_{jA\alpha} \tag{D6}$$

as the order parameter for the intermediate phase, which can be evaluated for each magnetic unit cell j. Note that the

last term ensures $\sigma_{1,2,3}$ sum to zero. Such three numbers whose sum is a constant can be conveniently represented on a ternary plot. Since $\sigma_{1,2,3} \in [-1, 1]$, we first define rescaled variables

$$\tilde{\sigma}_\alpha \equiv \frac{\sigma_\alpha + 1}{3} \tag{D7}$$

so that $\tilde{\sigma}_1 + \tilde{\sigma}_2 + \tilde{\sigma}_3 = 1$. Then, the charge-ordered phase corresponds to $(\tilde{\sigma}_1, \tilde{\sigma}_2, \tilde{\sigma}_3) = (\frac{1}{3}, \frac{1}{3}, \frac{1}{3})$, and the partial-ordered phase $(\bar{\sigma}, -\bar{\sigma}, 0)$ corresponds to all permutations of $(\frac{1}{3}, \frac{2}{3}, 0)$ and their time reversal, which coincide with the former. For the other possible phases in the main text, $(\frac{\bar{\sigma}}{3}, \frac{2\bar{\sigma}}{3}, -\bar{\sigma}) \to (\frac{4}{9}, \frac{5}{9}, 0), (\frac{2}{9}, \frac{1}{9}, \frac{2}{3})$, $(\frac{\bar{\sigma}}{2}, \frac{\bar{\sigma}}{2}, -\bar{\sigma}) \to (\frac{1}{2}, \frac{1}{2}, 0)$, $(\frac{1}{6}, \frac{1}{6}, \frac{2}{3})$. The corresponding ternary plots are shown in Fig. 5 of the main text. Equation (D7) can be calculated by either averaging over the whole MC cell or locally in each magnetic unit cell.

APPENDIX F: RELEVANCE OF DISTORTED KAGOME LATTICE OF HoAgGe TO IDEAL KAGOME LATTICE SPIN ICE PHYSICS

In this appendix, we discuss any possible influences of the rotation distortion of the kagome lattice in HoAgGe on its relevance to general kagome spin ice physics.

The ground state of HoAgGe is characterized by three inequivalent Ho sites. This feature is mainly a result of the magnetic space group of the fully ordered $\sqrt{3} \times \sqrt{3}$ ground state of HoAgGe and does not necessarily suggest the crystal structure or the associated spin Hamiltonian are very different from that of ideal kagome spin ice.

As shown in Table 1 of Ref. [16], HoAgGe crystallizes in the space group P-62m (No. 189), featuring a single Ho site located on a distorted kagome lattice. This structural distortion nonetheless breaks the spatial inversion symmetry. Below $T_2 = 11.6$ K, the magnetic ordering emerges with a propagation vector $k = (1/3, 1/3, 0)$, leading to the establishment of the MSG P-6′m2′ and an enlarged $\sqrt{3} \times \sqrt{3}$ magnetic unit cell. Describing such an ordered spin state requires three inequivalent Ho sites.

To see how different the situation is on an ideal kagome lattice, we consider an *imaginary* "ideal" stacked kagome spin ice, using the structure of FeSn as an example.

FeSn crystallizes in the space group P6/mmm (No. 191), with Fe atoms forming an ideal kagome lattice [89,90]. Under the assumption of a magnetic propagation vector $k = (1/3, 1/3, 0)$, the ground-state magnetic configurations of a fictitious kagome spin ice formed by spins on the Fe sites are shown in Fig. 19. The corresponding magnetic space groups compatible with both the crystal symmetry and the ordering wave vector are presented in Fig. 20. The $\sqrt{3} \times \sqrt{3}$ ground state, having the MSG P6′/m′mm′, still has two inequivalent Fe sites (see Fig. 19). Within the $\sqrt{3} \times \sqrt{3}$ magnetic unit cell [indicated by the blue rhombus in Fig. 19(a)], the three Fe2 positions are related by threefold rotational symmetry around the c axis, while the six Fe1 positions are connected through a combination of threefold rotation about the c axis and in-plane twofold rotational symmetry. In simple terms, having inequivalent sites in the magnetically ordered state should not be used as a criterion for the kagome ice system being unideal.

It is nonetheless worth figuring out the origin of the three inequivalent sites compared to two. As illustrated in Fig. 20, the MSG P-6′m2′ is a subgroup of P6′/m′mm′, with equivalent Ho sites related by threefold rotation around the c axis. Consequently, the two inequivalent Fe sites in the MSG P6′/m′mm′ are split into three inequivalent Ho sites in the MSG P-6′m2′ due to the structural distortion. The effect of this structural symmetry breaking is encoded in the different J_2 and J_4 values of the spin model, and, as shown in the main text, does not qualitatively change the ordering behavior of 2D and 3D kagome spin ice.

It is noteworthy that HoAgGe may undergo a first-order phase transition at T_2, which could render the three Ho sites inequivalent in the presence of strong

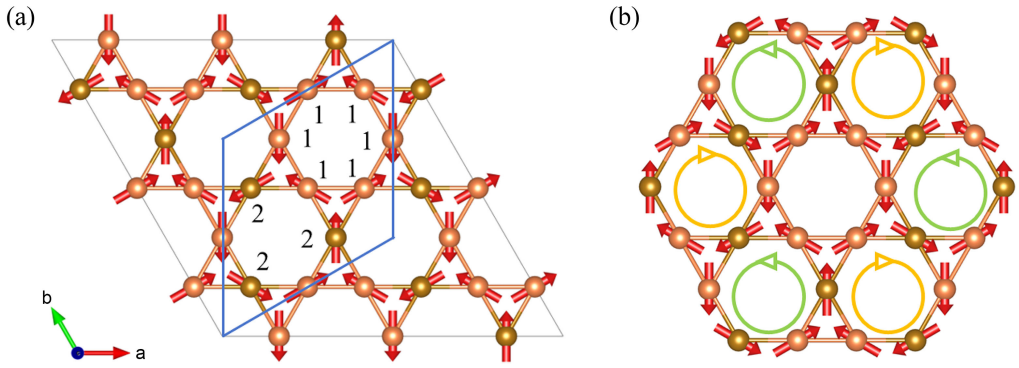

FIG. 19. Proposed magnetic structures of hypothetical kagome spin ice in FeSn. (a) Magnetic unit cell indicated by the blue rhombus, with the two inequivalent Fe sites Fe1 and Fe2 labeled by 1 and 2, respectively, for simplicity. (b) Clockwise and counterclockwise hexagons of spins in the expected ground state of kagome spin ice.

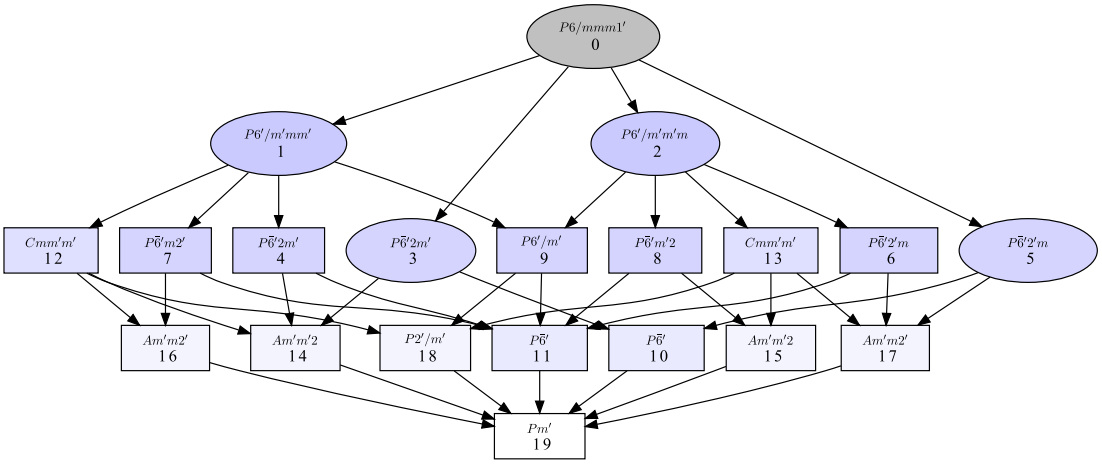

FIG. 20. The k-maximal symmetries (dark blue ellipse) and possible subgroups (rectangular box) that we refined for magnetic ordering of the Fe moment with propagation vector $k = (1/3, 1/3, 0)$ from the paramagnetic phase with P6/mmm symmetry (gray ellipse).

spin-phonon coupling. According to recent explicit Raman measurements [28], the magnitude of the phonon softening between T_1 and T_2 is about 0.2 cm^{-1} in HoAgGe, associated with the development of a large ordered magnetic moment. The estimated spin-phonon coupling constant in HoAgGe is approximately 0.02 cm^{-1}, an order of magnitude smaller than those observed in typical antiferromagnets such as FeF_2 and MnF_2, where the values average around 0.3–0.4 cm^{-1} [91], and significantly smaller than that of $ZnCr_2O_4$, which exhibits a coupling constant of about 5 cm^{-1} [92]. As discussed above, the transition at T_2 has been identified as a second-order transition belonging to the 3D XY universality class, coinciding with a magnetic charge crossover at T_1, with no clear evidence supporting a first-order transition in HoAgGe.

[1] L. Balents, *Spin liquids in frustrated magnets*, Nature (London) **464**, 199 (2010).

[2] C. Broholm, R. J. Cava, S. A. Kivelson, D. G. Nocera, M. R. Norman, and T. Senthil, *Quantum spin liquids*, Science **367**, eaay0668 (2020).

[3] M. J. Harris, S. T. Bramwell, D. F. McMorrow, T. Zeiske, and K. W. Godfrey, *Geometrical frustration in the ferromagnetic pyrochlore* $Ho_2Ti_2O_7$, Phys. Rev. Lett. **79**, 2554 (1997).

[4] A. P. Ramirez *et al.*, *Zero-point entropy in 'spin ice'*, Nature (London) **399**, 333 (1999).

[5] S. T. Bramwell and M. J. P. Gingras, *Spin ice state in frustrated magnetic pyrochlore materials*, Science **294**, 1495 (2001).

[6] C. Castelnovo, R. Moessner, and S. L. Sondhi, *Magnetic monopoles in spin ice*, Nature (London) **451**, 42 (2008).

[7] L. Pauling, *The structure and entropy of ice and of other crystals with some randomness of atomic arrangement*, J. Am. Chem. Soc. **57**, 2680 (1935).

[8] D. J. P. Morris *et al.*, *Dirac strings and magnetic monopoles in the spin ice* $Dy_2Ti_2O_7$, Science **326**, 411 (2009).

[9] T. Fennell *et al.*, *Magnetic Coulomb phase in the spin ice* $Ho_2Ti_2O_7$, Science **326**, 415 (2009).

[10] M. Wolf and K. D. Schotte, *Ising model with competing next-nearest-neighbour interactions on the Kagome lattice*, J. Phys. A **21**, 2195 (1988).

[11] T. Takagi and M. Mekata, *Magnetic ordering of Ising spins on kagomé lattice with the 1st and the 2nd neighbor interactions*, J. Phys. Soc. Jpn. **62**, 3943 (1993).

[12] A. S. Wills, R. Ballou, and C. Lacroix, *Model of localized highly frustrated ferromagnetism: The kagomé spin ice*, Phys. Rev. B **66**, 144407 (2002).

[13] G. Möller and R. Moessner, *Magnetic multipole analysis of kagome and artificial spin-ice dipolar arrays*, Phys. Rev. B **80**, 140409(R) (2009).

[14] G.-W. Chern, P. Mellado, and O. Tchernyshyov, *Two-stage ordering of spins in dipolar spin ice on the kagome lattice*, Phys. Rev. Lett. **106**, 207202 (2011).

[15] G.-W. Chern and O. Tchernyshyov, *Magnetic charge and ordering in kagome spin ice*, Phil. Trans. R. Soc. A **370**, 5718 (2012).

[16] K. Zhao *et al.*, *Realization of the kagome spin ice state in a frustrated intermetallic compound*, Science **367**, 1218 (2020).

[17] K. Zhao *et al.*, *Discrete degeneracies distinguished by the anomalous Hall effect in a metallic kagome ice compound*, Nat. Phys. **20**, 442 (2024).

[18] L. Anghinolfi *et al.*, *Thermodynamic phase transitions in a frustrated magnetic metamaterial*, Nat. Commun. **6**, 8278 (2015).

[19] Benjamin Canals *et al.*, *Fragmentation of magnetism in artificial kagome dipolar spin ice*, Nat. Commun. **7**, 11446 (2016).

[20] M. E. Brooks-Bartlett, S. T. Banks, L. D. C. Jaubert, A. Harman Clarke, and P. C. W. Holdsworth, *Magnetic-moment fragmentation and monopole crystallization*, Phys. Rev. X **4**, 011007 (2014).

[21] Yao Wang, Stephan Humeniuk, and Yuan Wan, *Tuning the two-step melting of magnetic order in a dipolar kagome spin ice by quantum fluctuations*, Phys. Rev. B **101**, 134414 (2020).

[22] Wen-Yu Su, Feng Hu, Chen Cheng, and Nvsen Ma, *Berezinskii-Kosterlitz-Thouless phase transitions in a kagome spin ice by a quantifying Monte Carlo process: Distribution of Hamming distances*, Phys. Rev. B **108**, 134422 (2023).

[23] Eric C. Andrade and Matthias Vojta, *Partial magnetic order in kagome spin ice*, Phys. Rev. B **109**, L241102 (2024).

[24] N. Li *et al.*, *Low-temperature transport properties of the intermetallic compound HoAgGe with a kagome spin-ice state*, Phys. Rev. B **106**, 014416 (2022).

[25] S. Roychowdhury *et al.*, *Enhancement of the anomalous Hall effect by distorting the Kagome lattice in an antiferromagnetic material*, Proc. Natl. Acad. Sci. U.S.A. **121**, 01970 (2024).

[26] H. B. Deng *et al.*, *Local excitation of kagome spin ice magnetism seen by scanning tunneling microscopy*, Phys. Rev. Lett. **133**, 046503 (2024).

[27] Hari Bhandari *et al.*, *Tunable topological transitions in the frustrated magnet* HoAgGe, Commun. Mater. **6**, 52 (2025).

[28] S. Wu, L. Zhao, W. Song, M. Tan, F. Jin, T. Ying, J. X. Yin, and Q. Zhang, *Lattice dynamics and spin-phonon coupling in the kagome spin ice HoAgGe*, Phys. Rev. B **111**, 125116 (2025).

[29] F. Schilberth *et al.*, *Large magnetoreflectance and optical anisotropy due to* $4f$ *flat bands in the frustrated kagome magnet HoAgGe*, arXiv:2504.10274.

[30] G. F. Schwertfeger, P. H. Chang, P. Nikolic, and I. I. Mazin, *Modeling of a twisted kagome* HoAgGe *spin ice using reduced configuration space search and density functional theory*, Phys. Rev. B **112**, 214411 (2025).

[31] Jiyuan Li *et al.*, *Complex magnetic phase diagram of the metallic kagome ice* HoAgGe, Phys. Rev. B **112**, 224426 (2025).

[32] Y. Tabata, H. Kadowaki, K. Matsuhira, Z. Hiroi, N. Aso, E. Ressouche, and B. Fak, *kagomé ice state in the dipolar spin ice* $Dy_2Ti_2O_7$, Phys. Rev. Lett. **97**, 257205 (2006).

[33] T. Fennell *et al.*, *Pinch points and Kasteleyn transitions in kagome ice*, Nat. Phys. **3**, 566 (2007).

[34] A. A. Turrini, A. Harman Clarke, G. Haeseler, T. Fennell, I. G. Wood, P. Henelius, S. T. Bramwell, and P. C. W. Holdsworth, *Tunable critical correlations in kagome ice*, Phys. Rev. B **105**, 094403 (2022).

[35] Y. Qi, T. Brintlinger, and J. Cumings, *Direct observation of the ice rule in an artificial kagome spin ice*, Phys. Rev. B **77**, 094418 (2008).

[36] E. Mengotti *et al.*, *Real-space observation of emergent magnetic monopoles and associated Dirac strings in artificial kagome spin ice*, Nat. Phys. **7**, 68 (2011).

[37] C. Nisoli, R. Moessner, and P. Schiffer, *Colloquium: Artificial spin ice: Designing and imaging magnetic frustration*, Rev. Mod. Phys. **85**, 1473 (2013).

[38] R. Shindou and N. Nagaosa, *Orbital ferromagnetism and anomalous Hall effect in antiferromagnets on the distorted fcc lattice*, Phys. Rev. Lett. **87**, 116801 (2001).

[39] Y. Taguchi *et al.*, *Spin chirality, Berry phase, and anomalous hall effect in a frustrated ferromagnet*, Science **291**, 2573 (2001).

[40] Y. Machida *et al.*, *Time-reversal symmetry breaking and spontaneous Hall effect without magnetic dipole orderm*, Nature (London) **463**, 210 (2010).

[41] H. Chen, Q. Niu, and A. H. MacDonald, *Anomalous Hall effect arising from noncollinear antiferromagnetism*, Phys. Rev. Lett. **112**, 017205 (2014).

[42] S. Nakatsuji *et al.*, *Large anomalous Hall effect in a noncollinear antiferromagnet at room temperature*, Nature (London) **527**, 212 (2015).

[43] Z. Q. Liu *et al.*, *Electrical switching of the topological anomalous Hall effect in a non-collinear antiferromagnet above room temperature*, Natl. Electron. Rev. **1**, 172 (2018).

[44] K. Zhao, T. Hajiri, H. Chen, R. Miki, H. Asano, and P. Gegenwart, *Anomalous Hall effect in the noncollinear antiferromagnetic antiperovskite* $Mn_3Ni_{1-x}Cu_xN$, Phys. Rev. B **100**, 045109 (2019).

[45] H. Chen, *Electronic chiralization as an indicator of the anomalous Hall effect in unconventional magnetic systems*, Phys. Rev. B **106**, 024421 (2022).

[46] R. R. Birss and J. C. Anderson, *Linear magnetostriction in antiferromagnetics*, Proc. Phys. Soc. London **81**, 1139 (1963).

[47] G. Gorodetsky, B. Sharon, and S. Shtrikman, *Linear effect of the magnetic field on the magnetic susceptibility in antiferromagnetic* $DyFeO_3$, Solid State Commun. **5**, 739 (1967).

[48] M. Blume, L. M. Corliss, J. M. Hastings, and E. Schiller, *Observation of an antiferromagnet in an induced staggered magnetic field: Dysprosium aluminum garnet near the tricritical point*, Phys. Rev. Lett. **32**, 544 (1974).

[49] J. F. Dillon, E. Y. Chen, N. Giordano, and W. P. Wolf, *Time-reversed antiferromagnetic states in dysprosium aluminum garnet*, Phys. Rev. Lett. **33**, 98 (1974).

[50] R. Alben, M. Blume, L. M. Corliss, and J. M. Hastings, *Induced staggered magnetic fields in antiferromagnets*, Phys. Rev. B **11**, 295 (1975).

[51] N. Giordano and W. P. Wolf, *Induced staggered magnetic fields in antiferromagnets: Microscopic mechanisms*, Phys. Rev. B **21**, 2008 (1980).

[52] W. Wolf, *Induced staggered field effects in antiferromagnets*, J. Magn. Magn. Mater. **90–91**, 197 (1990).

[53] T. C. Fujita, Y. Kozuka, M. Uchida, A. Tsukazaki, T. Arima, and M. Kawasaki, *Odd-parity magnetoresistance in pyrochlore iridate thin films with broken time-reversal symmetry*, Sci. Rep. **5**, 9711 (2015).

[54] Tian Liang, Timothy H. Hsieh, Jun J. Ishikawa, Satoru Nakatsuji, Liang Fu, and N. P. Ong, *Orthogonal magnetization and symmetry breaking in pyrochlore iridate* $Eu_2Ir_2O_7$, Nat. Phys. **13**, 599 (2017).

[55] Yilin Wang, Hongming Weng, Liang Fu, and Xi Dai, *Noncollinear magnetic structure, and multipolar order in* $Eu_2Ir_2O_7$, Phys. Rev. Lett. **119**, 187203 (2017).

[56] E. Lhotel *et al.*, *Evidence for dynamic kagome ice*. Nat. Commun. **9**, 3786 (2018).

[57] J. Xu *et al.*, *Anisotropic exchange Hamiltonian, magnetic phase diagram, and domain inversion of* $Nd_2Zr_2O_7$, Phys. Rev. B **99**, 144420 (2019).

[58] Aloysius P. Gottlob and Martin Hasenbusch, *Critical behaviour of the 3D XY-model: A Monte Carlo study*, Physica (Amsterdam) **201A**, 593 (1993).

[59] Seiji Miyashita, *Nature of the ordered phase, and the critical properties of the three dimensional six-state clock model*, J. Phys. Soc. Jpn. **66**, 3411 (1997).

[60] J. Lou, A. W. Sandvik, and L. Balents, *Emergence of U(1) symmetry in the 3D XY model with Zq anisotropy*, Phys. Rev. Lett. **99**, 207203 (2007).

[61] M. E. Fisher, *Renormalization Group in Critical Phenomena, and Quantum Field Theory*, edited by J. Gunton and M. S. Green (Temple University, Philadelphia, 1975).

[62] D. R. Nelson, *Coexistence-curve singularities in isotropic ferromagnets*, Phys. Rev. B **13**, 2222 (1976).

[63] D. J. Amit and L. Peliti, *On dangerously irrelevant operators*, Ann. Phys. (N.Y.) **140**, 207 (1982).

[64] H. Shao, W. Guo, and A. W. Sandvik, *Monte Carlo renormalization flows in the space of relevant and irrelevant operators: Application to three-dimensional clock models*, Phys. Rev. Lett. **124**, 080602 (2020).

[65] Samuel V. Gallego, Jesus Etxebarria, Luis Elcoro, Emre S. Tasci, and J. Manuel Perez-Mato, *Automatic calculation of symmetry-adapted tensors in magnetic and non-magnetic materials: A new tool of the bilbao crystallographic server*, Acta Crystallogr. Sect. A **75**, 438 (2019).

[66] Mois Ilia Aroyo, Juan Manuel Perez-Mato, Cesar Capillas, Eli Kroumova, Svetoslav Ivantchev, Gotzon Madariaga, Asen Kirov, and Hans Wondratschek, *Bilbao crystallographic server: I. databases, and crystallographic computing programs*, Z. Kristallogr.-Cryst. Mater. **221**, 15 (2006).

[67] Mois I. Aroyo, Asen Kirov, Cesar Capillas, J. M. Perez-Mato, and Hans Wondratschek, *Bilbao crystallographic server. ii. representations of crystallographic point groups and space groups*, Acta Crystallogr. Sect. A **62**, 115 (2006).

[68] S. Lucas *et al.*, *Entropy evolution in the magnetic phases of partially frustrated* CePdAl, Phys. Rev. Lett. **118**, 107204 (2017).

[69] G. M. Schmiedeshoff *et al.*, *Multiple regions of quantum criticality in* YbAgGe, Phys. Rev. B **83**, 180408(R) (2011).

[70] J. F. Allen and A. D. Misener, *Flow of liquid helium II*, Nature (London) **141**, 75 (1938).

[71] P. Kapitza, *Viscosity of liquid helium below the λ-point*, Nature (London) **141**, 74 (1938).

[72] J. A. Lipa, D. R. Swanson, J. A. Nissen, T. C. P. Chui, and U. E. Israelsson, *Heat capacity and thermal relaxation of bulk helium very near the lambda point*, Phys. Rev. Lett. **76**, 944 (1996).

[73] J. A. Lipa, J. A. Nissen, D. A. Stricker, D. R. Swanson, and T. C. P. Chui, *Specific heat of liquid helium in zero gravity very near the lambda point*, Phys. Rev. B **68**, 174518 (2003).

[74] M. Campostrini, M. Hasenbusch, A. Pelissetto, and E. Vicari, *Theoretical estimates of the critical exponents of the superfluid transition in* ^{4}He *by lattice methods*, Phys. Rev. B **74**, 144506 (2006).

[75] Ti-Yen Lan, Yun-Da Hsieh, and Ying-Jer Kao, *High-precision Monte Carlo study of the three-dimensional XY model on GPU*, arXiv:1211.0780.

[76] E. Morosan, S. L. Bud'ko, P. C. Canfield, M. S. Torikachvili, and A. H. Lacerda, *Thermodynamic and transport properties of RAgGe (*R = Tb − Lu*) single crystals*, J. Magn. Magn. Mater. **277**, 298 (2004).

[77] R. Kuchler, T. Bauer, M. Brando, and F. Steglich, *A compact and miniaturized high resolution capacitance dilatometer for measuring thermal expansion and magnetostriction*, Rev. Sci. Instrum. **83**, 095102 (2012).

[78] R. Kuchler, A. Worl, P. Gegenwart, M. Berben, B. Bryant, and S. Wiedmann, *The world's smallest capacitive dilatometer, for high-resolution thermal expansion and magnetostriction in high magnetic fields*, Rev. Sci. Instrum. **88**, 083903 (2017).

[79] R. Prozorov and V. G. Kogan, *Effective demagnetizing factors of diamagnetic samples of various shapes*, Phys. Rev. Appl. **10**, 014030 (2018).

[80] V. Hutanu, *POLI: Polarised hot neutron diffractometer*, J. Large-Scale Res. Facil. **1**, A16 (2015).

[81] H. Thoma, W. Luberstetter, J. Peters, and V. Hutanu, *Polarised neutron diffraction using novel high-Tc superconducting magnet on single crystal diffractometer POLI at MLZ*, J. Appl. Crystallogr. **51**, 17 (2018).

[82] V. Petříček, M. Dušek, and L. Palatinus, *Crystallographic computing system JANA2006: General features*, Z. Kristallogr. **229**, 345 (2014).

[83] S. V. Gallego, E. S. Tasci, G. de la Flor, J. M. Perez-Mato, and M. I. Aroyo, *Magnetic symmetry in the Bilbao Crystallographic Server: A computer program to provide systematic absences of magnetic neutron diffraction*, J. Appl. Crystallogr. **45**, 1236 (2012).

[84] H. T. Stokes and D. M. Hatch, *FINDSYM: Program for identifying the space-group symmetry of a crystal*, J. Appl. Crystallogr. **38**, 237 (2005).

[85] Yixi Su, *DNS: Diffuse scattering neutron time-of-flight spectrometer*, J. Large-Scale Res. Facil. **1**, A27 (2015).

[86] D. A. Keen, M. J. Gutmann, and C. C. Wilson, *SXD – the single-crystal diffractometer at the ISIS spallation neutron source*, J. Appl. Crystallogr. **39**, 714 (2006).

[87] Nicholas Metropolis, Arianna W. Rosenbluth, Marshall N. Rosenbluth, Augusta H. Teller, and Edward Teller, *Equation of state calculations by fast computing machines*, J. Chem. Phys. **21**, 1087 (1953).

[88] A. W. Sandvik, *Computational studies of quantum spin systems*, AIP Conf. Proc. **1297**, 135 (2010).

[89] M. Kang *et al.*, *Dirac fermions and flat bands in the ideal kagome metal* FeSn, Nat. Mater. **19**, 163 (2020).

[90] Nirmal J. Ghimire and Igor I. Mazin, *Topology and correlations on the kagome lattice*, Nat. Mater. **19**, 137 (2020).

[91] D. J. Lockwood and M. G. Cottam, *The spin-phonon interaction in* FeF_2 *and* MnF_2 *studied by Raman spectroscopy*, J. Appl. Phys. **64**, 5876 (1988).

[92] Ch. Kant, J. Deisenhofer, T. Rudolf, F. Mayr, F. Schrettle, A. Loidl, V. Gnezdilov, D. Wulferding, P. Lemmens, and V. Tsurkan, *Optical phonons, spin correlations, and spin-phonon coupling in the frustrated pyrochlore magnets* $CdCr_2O_4$ *and* $ZnCr_2O_4$, Phys. Rev. B **80**, 214417 (2009).